CPO and quantitative textural analyses within sheath folds

DOI:10.1016/j.jsg.2023.105000

Journal of Structural Geology

CPO and quantitative textural analyses within sheath folds

--Manuscript Draft--

Manuscript Number:	SG-D-23-00223
Article Type:	VSI: Innovations_geoscience
Keywords:	Sheath fold; EBSD; ND; CPO; 3D modelling; Scottish Caledonides
Abstract:	We investigate the intra- and inter-crystalline deformation processes involved in sheath fold development combining complementary fabric analysis techniques and 3D modelling by neutron tomography. The investigated sheath fold is a multi-layered sub-metre scale single-eye structure developed in psammites from the Moine Nappe overlying the Moine Thrust Zone of NW Scotland. Crystallographic Preferred Orientations (CPOs) of quartz and biotite were acquired through a Neutron Diffractometer and an SEM-EBSD system to compare the full-fabric of the main phases and the active slip systems for an "in situ" structural control. Combined with orientation maps and grain size maps, results show that, despite the different structural positions of the investigated microdomains (upper vs lower fold limbs, inner vs outer sheath closures, distance from hinge of the sheath fold), quartz and biotite deformed uniformly, suggesting a constant differential stress and orientation of the kinematic vorticity axis. Previously recognised detachment horizons within the sampled sheath fold do not affect the fabric patterns recorded by quartz and biotite. This may be interpreted in two different ways: i) detachments formed during earlier active folding and prior to passive amplification of folds associated with more uniform flow to create the sheath fold geometries; ii) the quartz c-axis patterns are coeval with a late deformation phase (loading of the orogenic wedge) that pervasively obliterated the previous fabric and therefore did not preserve the active folding component. Several pieces of evidence reported here such as top-to-SE normal-shear sense which is opposite to the regional kinematics are more in line with the second hypothesis. Evaluating the texture of minerals provides an improved dataset for the whole sheath fold and increases our understanding of recrystallization mechanisms active in shear zones.

CPO and quantitative textural analyses within sheath folds

Fazio, E.[1]*, Alsop, G.I.[2], Nania, L.[3], Graziani, R.[3], Iaccarino, S.[4], Montomoli, C.[4], Carosi, R.[4], Luzin, V.[5], Salvemini F.[5], Gambino, S.[1], Cirrincione, R.[1], Mamtani, M.A.[6]

[1] Dipartimento Scienze Biologiche Geologiche e Ambientali, Università di Catania, Italy
[2] School of Geosciences, University of Aberdeen, Aberdeen, AB24 3UE, United Kingdom
[4] Geological Survey of Canada, Natural Resources Canada, Ottawa, Canada
[4] Dipartimento Scienze della Terra, Università di Torino, Italy
[5] Australian Nuclear Science and Technology Organization (ANSTO), Lucas Heights, NSW, Australia
[6] Department of Geology & Geophysics, Indian Institute of Technology, Kharagpur-721302, West Bengal, India

* *Corresponding email:* eugenio.fazio@unict.it

Abstract

We investigate the intra- and inter-crystalline deformation processes involved in sheath fold development combining complementary fabric analysis techniques and 3D modelling by neutron tomography. The investigated sheath fold is a multi-layered sub-metre scale single-eye structure developed in psammites from the Moine Nappe overlying the Moine Thrust Zone of NW Scotland. Crystallographic Preferred Orientations (CPOs) of quartz and biotite were acquired through a Neutron Diffractometer and ~~an~~ SEM-EBSD system to compare the full-fabric of the main phases and the active slip systems for an "in situ" structural control. Combined with orientation maps and grain size maps, results show that, despite the different structural positions of the investigated microdomains (upper vs lower fold limbs, inner vs outer sheath closures, distance from hinge of the sheath fold), quartz and biotite deformed uniformly, suggesting a constant differential stress and orientation of the kinematic vorticity axis. Previously recognised detachment horizons within the sampled sheath fold do not affect the fabric patterns recorded by quartz and biotite. This may be interpreted in two different ways: i) detachments formed during earlier active folding and prior to passive amplification of folds associated with more uniform flow to create the sheath fold geometries; ii) the quartz c-axis patterns are coeval with a late deformation phase (loading of the orogenic wedge) that pervasively obliterated the previous fabric and therefore did not preserve the active folding component. Several pieces of evidence reported here such as top-to-SE normal-shear sense which is opposite to the regional kinematics are more in line with the second hypothesis. Evaluating the texture of minerals provides an improved dataset for the whole sheath fold and increases our understanding of recrystallization mechanisms active in shear zones.

Keywords: Sheath fold, EBSD, ND, CPO, 3D modelling

Highlights

- We investigate the 3D geometry and kinematics to determine potential flow variation within sheath folds
- CPOs of quartz and biotite are acquired through a Neutron Diffractometer and an SEM-EBSD system
- CPO maintains constant shear sense throughout the fold with no evidence of active folding preserved
- Top-to-SE normal-shear sense within the sheath fold is opposite to the regional thrust kinematics and suggests a late phase of peak temperature extension.

Graphical abstract

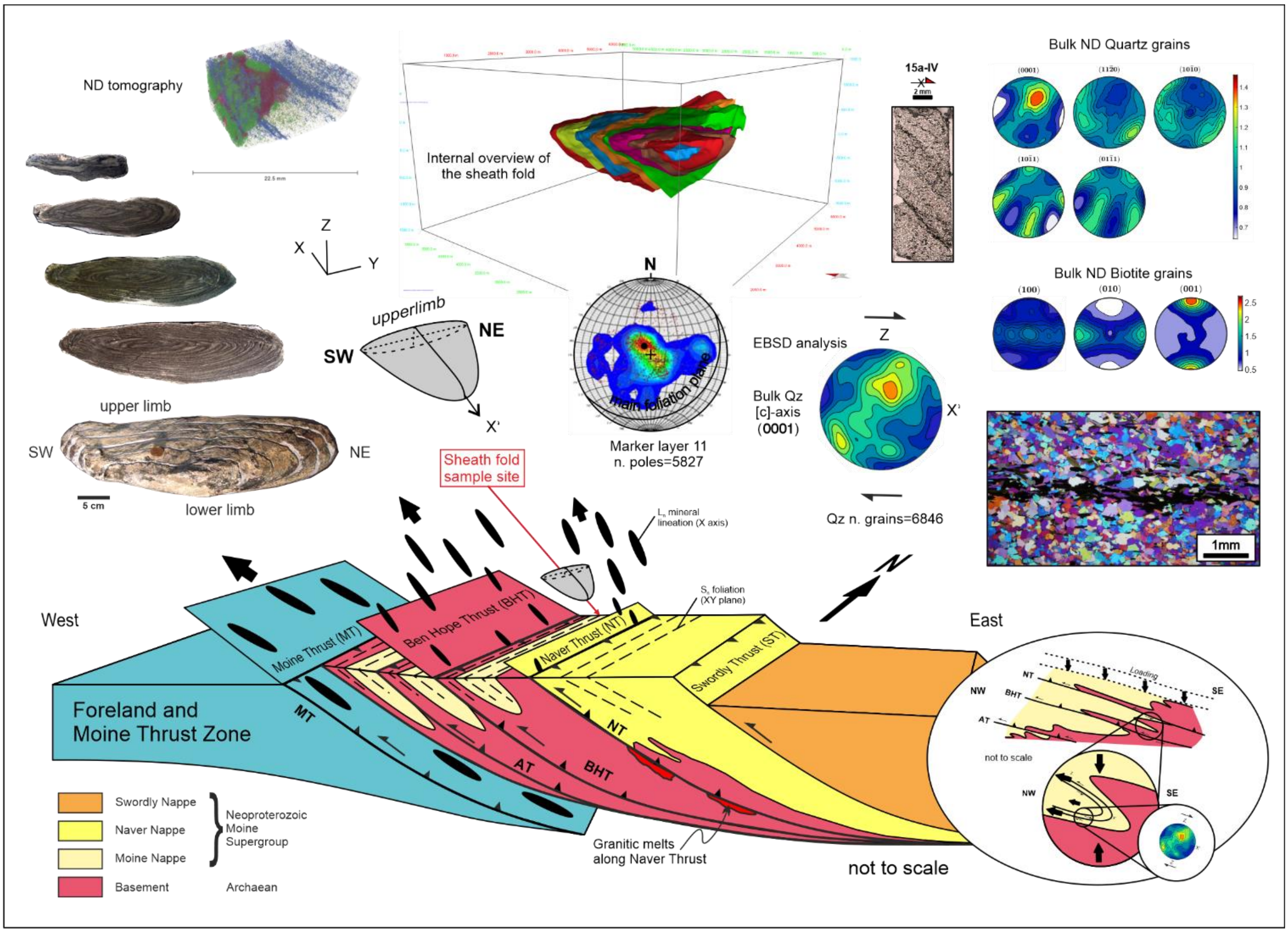

1. Introduction

Sheath folds are curved tongue-shaped non-cylindrical structures with cross sections across fold noses revealing elliptical-shaped rings or 'eyes' developed during deformation (e.g., Carreras et al., 1977; Quinquis et al., 1978; Minnigh, 1979; Cobbold and Quinquis, 1980; Ramsay, 1980). The hinge line is curved through more than 90 degrees (Ramsay and Huber, 1987; Passchier and Trouw, 2005), with the apex of the sheath generally oriented parallel to the direction of maximum elongation (i.e., X axes of the strain ellipsoid; Alsop and Holdsworth, 2007). The main structural features of sheath folds are briefly summarized as follows: i) they have a conical- or tongue-shape, with limbs closing toward the apex and ii) sections parallel to the YZ plane show a characteristic circular/elliptical shape forming eye-type folds (for a comprehensive overview of sheath folds, their formation, and characteristics refer to Alsop et al., 2007; Alsop and Holdsworth, 2007; 2012). Their widespread occurrence makes them a crucial source of information to understand the processes of plastic deformation and shaping of the Earth's crust. Yet, how the material is passively or actively deformed, , defined as where layering has no control or affects resulting sheath fold geometries respectively (see Alsop and Holdsworth, 2012), and how different minerals affect their development is poorly constrained. Passive sheath folding is defined as where the layering plays no part in the mechanics of the folding process (e.g. Cobbold and Quinquis, 1980, p.120), with the sense of shear remaining constant around the fold and across its axial surface (Alsop and Holdsworth, 2012).Conversely, active sheath folding is marked by "heterogeneous deformation in which rheologically distinct layering results in the development of local discontinuities about the sheath closure" (Alsop and Holdsworth, 2012, p.110). In order to address these issues, we investigate the intracrystalline processes behind sheath fold development through a detailed study of the main rock forming minerals by means of complementary fabric analyses and 3D modelling using neutron tomography.

Sheath folds can form in a variety of tectonic settings, and have been widely reported around the world, including Cap de Creus (Alsop and Carreras et al., 2007; Druguet et al., 2009; Carreras and Druguet, 2019), the Scottish Highlands (Alsop and Holdsworth, 2006), the Appalachian Mountains in the eastern United States (Merschat et al., 2005), the Scandinavian Caledonides (Passchier and Trouw, 2005), the Arctic zone of the Palaeoproterozoic north-eastern Fennoscandian Shield (Mudruk et al., 2022), the Alps (Maino et al., 2021), the Calabrian-Peloritani Orogen in southern Italy (Fazio et al., 2018; Ortolano et al., 2020), the Oman Mountains (Searle and Alsop, 2007), the Himalayan orogen in Asia, as well as several Precambrian terrains (e.g., Ghosh et al., 1999). Sheath folds can also develop in other materials (e.g. ice; Bons et al. 2016) or settings such as salt basins where horizontal flow of salt (e.g. Fiduk and Rowan, 2012; Pérez et al, 2017) or vertical rise of salt (diapirism) leads to concentrated shear stresses within salt and along the interface between the salt and the adjacent sedimentary rocks (e.g., Jackson et al., 1994; Rowan and Vendeville, 2006; Hudec and Jackson, 2007; for a review see Alsop et al., 2007 and Carreras and Druguet, 2019). Most commonly, sheath folds are associated with deformation in mountain belts or convergent plate boundaries, but can also form in response to strike-slip faulting or extensional tectonics (Ramsay and Huber, 1987; Passchier and Trouw, 2005).

Sheath folds develop at a large range of scales (Fazio, 2019) spanning from millimetre-scale, as observed in thin sections (Rowe et al., 2005; Fazio et al., 2018) up to regional kilometre scale forming megafolds (Alsop, 1994; Searle and Alsop, 2007; Mudruk et al., 2022; for a review of sheath fold scales see Alsop et al., 2007). The widespread occurrence of sheath folds and their potential link between shape and strain are one of the main reasons why they have been widely studied in the past, both for tectonic implication and for relating regional high-strain structures with ore deposit distributions (Roberts, 1987; Park, 1988; Kampmann et al., 2016). Since Ramsay and Huber (1987), it has been suggested that sheath folds may develop around: 1) rigid objects within a more ductile rock matrix (Rosas et al., 2002), 2) slip surfaces (Reber et al., 2012, 2013a) or 3) weak inclusions (Reber et al., 2013b; Maino et al., 2021). In such cases, the internal profile of the structure is determined by the shape and size of the inclusion, as well as the deformation history of the surrounding rock (Ramsay, 1967; Carreras et al., 2005).

A number of authors (e.g., Carreras et al., 1977; Quinquis et al., 1978; Minnigh, 1979; Cobbold and Quinquis, 1980; Ramsay, 1980) have suggested that folds with gently curving hinge lines formed about the transport direction may have this curvature accentuated during progressive simple shear deformation that is universally applied across the fold, and results in highly curvilinear sheath folds geometries. The microstructural features of a sheath fold can therefore provide crucial information about the deformation paths of the involved layers and rocks. As a consequence, sheath fold shapes, mineral distributions, and orientations have been used to reconstruct the tectonic history of several regions. For example, map-scale sheath folds in the southern Appalachian of the eastern United States have been used to infer the orientation and magnitude of the bulk strain during mid-crustal flow of the metamorphic core (Merschat et al., 2005).

Along with the characterization of geometric features such as foliation or lineation (e.g., Alsop and Holdsworth, 2006; Alsop et al., 2007; Alsop and Holdsworth, 2012), crystallographic preferred orientation (CPO) of minerals (Fazio et al., 2010; Renjith et al., 2016; Hunter et al., 2018b; Graziani et al., 2020; Nania et al., 2022) is increasingly used to link micro-to-regional-scale deformation. CPO analyses potentially provides information on the orientation and magnitude of the deformation, as well as the rheological response of the rock. The CPO of minerals, particularly quartz and biotite, in metamorphic rocks can provide important information about the deformation history of the rock and the orientation of the strain ellipsoid. Quartz and biotite are both common minerals in medium to high-grade metamorphic rocks, and their crystal structures make them particularly sensitive to deformation. Under conditions of ductile deformation, quartz grains tend to elongate in the direction of maximum stretch and to re-orient accordingly to the active slip systems and deformation mechanism (e.g. Stipp et al., 2002; Toy et al., 2008; Morales et al., 2011b). This results in a strong CPO in which the c-axes of the quartz grains are preferentially oriented perpendicular to the direction of maximum shortening. Similarly, biotite grains tend to align their basal planes perpendicular to the direction of maximum shortening, resulting in a strong CPO (Punturo et al., 2017).

In sheath folds, the CPO of minerals is still poorly investigated, although is thought to be complex and varies between different parts of the fold (Morales et al., 2011a; Fazio et al., 2018). For example, in the axial region of the fold, quartz grains may exhibit a strong preferred orientation with respect to the fold axis, while on the limbs, the orientation may be more complex and reflect the influence of local finite strain gradients (Crispini and Capponi, 1997). Development of sheath folds and potential triggers for the process have been hypothesized in the literature (e.g., Cobbold and Quinquis, 1980; Reber et al. 2012; Carreras and Druguet, 2019), but rarely take account of intracrystalline deformation and rheological behaviour of mineral for their CPOs. Major studies on the orientation of minerals have been performed using optical methods, such as U-Stage and fabric analyzer

(Schmid and Casey, 1986; Stünitz, 1991; Crispini and Capponi, 1997), and SEM-EBSD-based systems (Morales et al., 2011a). These studies have been carried out for limited sampling or grain statistics, mostly due to the limitation of the techniques available at the time. Nowadays spatially resolved EBSD data can be combined with Neutron Diffraction allowing more robust statistical analyses of mineral CPO (e.g., Wilson et al., 2022).

The main research questions we pose in this study are therefore:

a) How does the deformation path vary (or not) within a multi-layer sheath fold?
b) Do fabric and flow variations develop in different structural positions within a sheath fold?
c) Can the CPO be used to determine if a sheath fold is propagating actively or passively?

To answer these questions and obtain a robust three-dimensional picture of a single sheath fold, we have analysed a metre-scale sheath fold originally sampled and described by Alsop and Holdsworth (2012). We explore its full fabric, combining detailed SEM-EBSD analyses on quartz and biotite with neutron diffraction (ND) texture analysis on a series of slices that were cut between the apex and body, and the inner and outer zones of the fold (Alsop and Holdsworth, 2012). We investigate quartz and biotite full CPOs; the deformation mechanisms of quartz; its relative differential stress; and how the kinematic vorticity axis (CVA; Michels et al., 2015) of the individual phases (quartz and biotite) and of the bulk was distributed as a function of the structural domain within the fold. This paper is one of the few studies of sheath folds employing detailed quantitative fabric analyses, thereby providing new insights into their development and propagation, with economic implications on the mineralization associated with large-scale sheath folds in metamorphic terranes.

2. Geological setting of the sample site

The northwestern extent of the (exposed) Scandian orogeny in Scotland is defined by the easterly-dipping Moine Thrust Zone that separates the foreland (in the west) from the early Neoproterozoic Moine Supergroup further east (Fig. 1a, b) (see Strachan et al. 2020 for a recent summary). The Moine Supergroup comprises a stack of east-dipping Scandian thrust nappes thought to be active at 437-415 Ma (Holdsworth et al. 1994; Strachan et al. 2010, 2020) which in the north coast of Scotland are defined by (from structurally lowest to highest) the Moine, Naver, Swordly and Skinsdale Thrusts (Fig. 1a, b). Additional thrusts exist within the Moine Nappe (Achinver and Ben Hope Thrusts) that do not separate distinct lithologies, although in the case of the Ben Hope Thrust may represent a thermal break (Thigpen et al., 2013, Ashley et al., 2015) (Fig. 1a, b).

The sheath fold sample used in this study was originally collected by Alsop and Holdsworth (2012) from psammites and pelites interlayered on a 10 cm scale, and which form part of the Moine Supergroup of northern Scotland (see details in Strachan et al., 2010; Strachan et al., 2020) (Fig. 1a, b, c). The sample site (UK Grid: NC6265857546) is in the upper part of the Moine Nappe (above the Ben Hope Thrust) in an area associated with top-to-the-NW-directed Scandian thrusting at 435-425 Ma (Holdsworth et al., 2001, 2006, 2007) (Fig. 1a, b, c). Sheath folds form from cm- to km-scales structures throughout the area and are marked by increasing non-coaxial deformation towards high strain zones (see Holdsworth et al., 2001; Alsop and Holdsworth, 1993; Alsop et al., 1996; 2010; 2021). The quartzo-feldspathic Moine psammites contain a regional foliation (Sn) defined by aligned quartz and biotite that dips towards the SE and a gently SE-plunging regional lineation (Ln) that are folded around the nose of the sampled sheath fold (Fig. 1c). The regional foliation (Sn) and lineation (Ln) developed during top-to-the-WNW regional D2 thrusting, with folding of these fabrics by the sheath fold suggesting that it formed relatively late (locally F3) during progressive D2 shearing (Alsop and Holdsworth, 1993, 2012; Alsop et al., 2010). The sampled sheath fold is a tight synform with a slightly steeper dipping upper limb, that closes towards the SE, and displays 120° of hinge-line curvature around the trend of the regional lineation (Ln). The sheath fold is considered to originally form the lower hinge of a NW-verging fold pair that are developed throughout the area (e.g., Holdsworth et al., 2001).

3. Materials and methods of textural analysis

The sample consisting of quartz-feldspar psammite was serially sectioned using a commercial rock saw with a 6 mm thick blade, at 15-20 mm intervals along the length (X axis) of the sheath fold and normal to the (X-Y) axial plane (Fig. 2; see Alsop and Holdsworth 2012 for details). The resulting eye-shaped closure patterns were then geometrically investigated by Alsop and Holdsworth (2012). We have now made thin sections from the sheath fold slices in different microdomains (Figs. 3-4) normal to the elongation (X axis of the finite strain ellipsoid) and at right angles to the (X-Y) axial plane (Fig. 2, 2f) for microstructural analysis.

A digital virtual 3D model was constructed using Move 2020.1.10 geomodelling software package (Petex Ltd.) using folded foliation planes manually traced on both sides of rock slices surfaces (i.e., markers' traces, Fig.2). The 3D model file is available as supplementary materials. Modelling was based on two orthogonal sections cutting across the sheath fold (x-y and x-z sections, representing the horizontal and vertical-longitudinal sections respectively, Fig. 2a) and 14 transversal slices (27 faces considering the front and back of each slice). To evaluate in detail the textural and kinematic variations recorded by quartz during folding, we analysed different portions of the sheath fold by electron backscatter diffraction (EBSD) and Neutron Diffraction (see Hunter et al., 2017a, b and Fazio et al. 2017 for comparison).

3.1. Electron Backscattered Diffraction

The EBSD analysis was carried out to acquire "in-situ" crystallographic orientations data of quartz and biotite as a function of the structural domain and to obtain quantitative grain size data. Thin section preparation for EBSD and initial petrographic imaging were carried out at the Fabric Analysis Lab (FAL), Department of Geology and Geophysics, Indian Institute of Technology (IIT), Kharagpur (India). Thirteen oriented thin sections approximating the XZ plane of the fabric (X parallel to mineral stretching lineation, Z normal to foliation plane) were investigated.

To obtain a damage free surface for EBSD analysis, the final stage of thin section preparation involved polishing with non-crystallizing colloidal silica solution for 6 hours. EBSD patterns were acquired at 30 kV accelerating voltage, 1.49 x 10-6 mbar system vacuum, and ~17 mm working distance using Carl Zeiss Auriga Compact FEG-SEM fitted with an Oxford instruments NordlysMax2 EBSD detector housed in the Central Research Facility (CRF, IIT Kharagpur, India). Quartz orientation data (Figs. 5-11) were acquired automatically using the software Aztec HKL (Oxford instruments). The data cleaning and initial processing was carried out using the software Aztec Crystal (Oxford instruments) while the final processing of the EBSD data was performed using the MTex toolbox (mtex-toolbox.github.io) for the software Matlab (www.mathworks.com). Grain size maps of quartz were produced along with lower hemisphere spherical equal area projections (pole figures) of the main crystallographic direction of quartz and biotite. The grain size maps were constructed using a grain boundary threshold of 10° to unambiguously highlight grain and subgrain boundaries (e.g., see Figs. 7a-d) while the pole figures were contoured using a de La Vallée Poussin kernel function with a halfwidth of 10°. A detailed study of the subgrain density was performed using the method proposed by Goddard et al. (2020) to quantify the intracrystalline differential stress. This analysis was done using a subgrain threshold of 1° a Burgers vector of $5.1x10^{-4}$ µm and a shear modulus of $4.2x10^{4}$ MPa (see Goddard et al., 2020 for more details). Density analyses on the peripheral areas of the quartz c-axis pole figures were carried out using the quantitative method of Hunter et al. (2018a).

3.2. Neutron Diffraction

Neutron Diffraction (ND) analyses were performed to refine and expand biotite and quartz textures from the EBSD dataset. Due to the neutron's large penetration capabilities (Feldmann, 1989; Vogel and Priesmeyer, 2006), the ND texture represents the bulk average texture over the whole sample volume, while the EBSD is limited to data from a single cross-section surface data. Thus, ND has the advantage over other techniques of large grain statistics and high fidelity of data. Investigation was performed at the Australian Centre for Neutron Scattering (ANSTO, Sydney). ND textural analysis has been performed on rock samples extracted from two slices, 15a and 17a (Figs. 12-13), to reconstruct volumetrically representative quartz and biotite CPOs. Small cubes approximately10x10x10 mm in size were extracted from different representative locations within the fold with potentially different deformation features and therefore textural characteristics (Figs. 12-13). A series of nine representative specimens allow us resolving the spatial distribution of deformation across the investigated fold.

Textural data have been acquired by means of the Kowari neutron diffractometer (for instrument reference see Garbe et al., 2015). For measurements of quartz and biotite multiple pole figures, the wavelength of 2.5Å and three detector (Bragg angle) position, 2θ = 39°, 64°, 92° (each with coverage ±7°) were used to acquire partial diffraction patterns covering the most desired diffraction peaks. As a result, 9 pole figures of quartz were extracted from the mentioned detector positions: (100), (101)/(011), (110), (102)/(012), (111), (112), (003), (202)/(022), (103)/(013) as well as several pole figures of biotite. All measurements were performed on a regular 35°×35° spherical grid to maximize the grain statistics – with such a fine mesh all grains in the sample are guaranteed to be detected.

The orientation distribution functions (ODFs) were reconstructed combining the ND orientation data for quartz and biotite in each sample using the MTex toolbox adopting the de La Vallée Poussin kernel function with a halfwidth of 10°. The following lattice parameters were adopted: a = b = 4.9 Å, c = 5.4 Å, α = β = 90°, λ = 120°, point group '321' for quartz; and a = 5.3 Å; b = 9.3 Å, c = 10 Å; α = λ = 90°, β = 100.23°, point group '12/m1'.

The lower hemisphere pole figures of the most relevant crystallographic axes and planes have been recalculated for quartz and biotite and plotted using the XZ plane of the finite strain ellipsoid as the projection plane, with a contouring halfwidth of 10°. For quartz and biotite CPOs intensities, the texture index (or J-index) of Bunge (1982) and the M-index of Skemer et al. (2005) were calculated (see Table 1 for EBSD data and Table S1 for Neutron Diffraction data).

3.3. Neutron Tomography

To characterize the three-dimensional bulk distribution of minerals in the series of nine cube samples, a neutron tomography (NT) study was conducted. The NT measurement was performed on the imaging beamline Dingo at ANSTO (Garbe et al., 2015). The high-resolution configuration, corresponding to a L/D ratio of 1000 (where L is the distance between the beam collimator to the image plane, and D the diameter of the collimator) was used. The analysis was conducted with a ZWO ASI2600MM Pro (6248*4176) CMOS sensor camera coupled with a 100 mm lens to yield images with a pixel size of 17 µm. The detector system was equipped with a 30µm thick Gd2O2S:Tb scintillation screen. The tomographic scan was carried out with an equiangular step of 0.17° over 360° and an exposure time of 90s each. Flat field normalization with dose correction, dark current subtraction, ring artefacts suppression in frequency and real space domains were applied to the raw data. The neutron tomography stacks were computed using the NeuTomPy toolbox (Micieli et al., 2019). The Avizo 2020.3.1 software was employed for data visualisation and evaluation (https://www.thermofisher.com/au/en/home/electron-microscopy/products/software-em-3d-vis/avizo-software.html accessed on 24 January 2023).

To enhance the quality of the NT image, anisotropic diffusion (AD) and unsharp mask (UM) filters were applied via AVIZO. The noise-reduction AD filter merges regions of similar grey-scale values and intra-region smoothing is promoted over edge smoothing. The blurring introduced by the AD filter was reduced by UM filter to reinforce the contrast at edges.

Different mineral phases can feature variations in neutron attenuation intensity that displays as grey-tone values in the NT reconstructed slices. Based on grey values, phases can be virtually separated through threshold segmentation. In the segmentation each pixel in the slice images composing the NT stack is assigned to a label which describes the region or minerals associated with the pixel (e.g., Qtz, K-feld, Bt) within a defined range of grey-tone values. Then the segmented components can be further manipulated and evaluated (Reddy, 2018).

4. **Results of microstructural and textural analysis**

4.1. Microstructures

The microstructural features of sheath folds, such as CPO and foliation, can provide valuable information about the orientation and magnitude of deformation, and can help unravel complex deformation histories (Ramsay and Huber, 1987; Passchier and Trouw, 2005). Polished thin sections were observed with the aid of optical microscopy. The main foliation (Sn-1) marked by micaceous layers forms the elliptical traces visible on YZ planes and is well developed in all investigated domains (Figs. 3-4). A secondary axial planar foliation (Sn) is developed mainly along the XY plane and consists of aligned elongated quartz grains and is highlighted by the shape preferred orientation of biotite flakes (Fig. 4a). There is no significant variation of microstructures, as well as of mineralogical assemblage and of minerals grain size, across the different slices. The studied psammite contains quartz, biotite, feldspars, white mica (phases are listed according to a decreasing of their relative modal abundance) with opaques, zircon, apatite and epidote as accessories phases. Minor chlorite is observed as alteration of biotite and sericite is locally observed in feldspars. Quartz shows evidence of dynamic recrystallization within the grain boundary migration I regime, GBM_I, of Stipp et al. (2002), as indicated by the occurrence of irregular, highly lobate grain boundaries (Fig. 4b) and of windows and pinning microstructures (Fig.4c). Quartz is only partly interconnected and often in contact with second phases (Fig, 5a, b; Fig. 6a, b), yet it defines a weak phase accommodating the deformation together with biotite. Quartz grain size is homogeneous within the sheath fold (see Fig. 6 for examples, see also supplementary materials A). Feldspars shows evidence of crystalline plasticity as highlighted by undulose extinction, deformation twins in plagioclase and locally myrmekite in K-feldspar (Fig. 4d).

4.2. CPO (integrated EBSD and ND textural analyses)

EBSD and ND can be considered two complementary techniques in the textural analysis of geomaterials. EBSD enables great analytical detail while maintaining structural control by examining "small" areas (one usually does not map more than an entire thin section for practical and time issues). With ND large volumes are analysed providing the full-fabric with greater statistics; however, without being able to verify which structural domains are being scanned within the volume (Fazio et al, 2017; Hunter et al., 2017b). This runs the risk of including grains that should be discarded from the calculation, such as those grains surrounded by second-phase minerals or those influenced by variations in the orientation of the 3D foliation plane. Comparing the two datasets is the best way to obtain a quantitative result while considering the heterogeneities of the sample. Moreover, ND is particularly suitable for acquiring the biotite fabric, as it avoids some indexing problems related to polishing (e.g., poor indexing, noise reduction, and pseudo-symmetry removal) and it investigates more crystals.

Quartz and biotite CPOs pole figures from EBSD (Figs. 7-9) and ND investigations (Figs. 12-13) show similar patterns, with no significant variations in the fabric strength (expressed by the J and M indexes) across the structure (Table 1, and Table S1). Quartz c-axis pole figures vary from single girdle/incomplete cross-girdle type 1 to hybrid of cleft-girdle and cross-girdle type 2 distributions (Figs. 7a-b, 8, 12, 13). Minor differences between CPOs from EBSD (Figs. 7-9) and ND analyses (Figs. 12-13) are related to grain statistics, and minor internal heterogeneities. We interpret quartz patterns as resulting from plane to constrictional strain (Schmid and Casey, 1986). Asymmetries of quartz CPOs all point to a top-to-the-SE (i.e. towards sheath fold apex parallel to the X direction) non-coaxial flow, regardless of the structural position (i.e., the apex to the body of the sheath fold; the outermost or the innermost ellipse, see Fig. 8).

The a-axis main maxima of quartz are preferentially oriented parallel to the lineation while the poles of r-planes are statistically oriented parallel to the pole of the foliation (Fig. 5a, b). The orientations of r-planes and a-axes within individual specimens (Fig. 5a, b) and for the bulk sheath fold (Fig. 9a) indicate a deformation by dislocation creep mainly accommodated by rhomb-a slip (for references, see Toy et al. 2008). The cross-girdle distribution of quartz c-axis and the distribution of low angle misorientation axes (Fig. 9c) also indicate the activity of other slip systems which can be identified as basal-a, and π-a (Neumann, 2000).

ND tomography reveals that in the various samples analyzed from different portions of the sheath fold, there is little variation in the phases present and the mineral volumes remain essentially unchanged within the volumes analyzed (Fig. 14; see supplementary materials for a complete dataset of ND tomography analyzed samples).

Biotite, defining the foliation within each specimen, is characterized by consistent EBSD and ND pole figures (Figs. 7c-d and Figs. 12-13). Couples of c-axis maxima (001) are sub-parallel to the sheath fold XY plane of the fabric, indicating variations of the internal foliation orientation across Y axis of the structure. Minor girdle distributions within the c-axis pole figures are normal to the internal foliations. The poles to the a-axes (100) and b-axes (010) define girdles distributions with sub-maxima of the b-axes parallel to the lineation. These distributions, especially considering the c-axis patterns, are constant (see also Fig. 9b for bulk biotite CPO), likely indicating a progressive growth of biotite during folding, with a stronger (re)crystallization at the last increment of deformation. Alternatively, biotite patterns could be associated with passive folding of the foliation during the development of the sheath fold.

4.3. Deformation temperature, paleo-stress estimates, and flow regime

Contoured pole figure symmetries of quartz c-axis patterns forming fabric ‘skeletons’ may be used as a geo-thermometer by analysing the opening angles between maxima of clustered orientations (Kruhl, 1996; Morgan and Law, 2004; Law, 2014). We applied the semi-quantitative method proposed by Hunter et al. (2018a) to compare the fabric intensity spectrum of girdles topologies. The quartz c-axis opening angles (measured by means of the open-source Matlab® toolbox MTEX – script modified after Hunter et al. (2018a) - for samples analysed through the EBSD, see Fig. 8) range from 84° to 87° with a single outlier of 100° (15a-IX). For a pressure of 4.5 kbar for the sheath fold thermal peak (estimated by Thigpen et al., 2013), the opening angles are representative of deformation temperatures of 570 ± 50°C to 580 ± 50°C (Table S2). The sample 15a-IX opening angle indicates a deformation temperature of 640 ± 50°C which is still in the overall error range of the other results. The opening angle of the bulk quartz CPO is likely underestimated as it accounts for the different rotations of the fabric skeleton of each rock slice. However, amphibolite facies deformation temperatures are also consistent with the GBM regime observed in the quartz (Stipp et al., 2002; Law, 2014) and by the ductile deformation in feldspars (see Passchier and Trouw, 2005). Similar temperature values have been also recently inferred by Southern et al. (2022) who studied elongated quartz pebbles in the Moine Nappe further to the northwest.

The crystallographic vorticity axis (CVA) of quartz and biotite in the individual samples and for the bulk sheath fold is located in the upper-right quadrant of the projection and is constant across the samples indicating no significant variations of the kinematic flow (Fig. 10). Results from subgrain piezometry indicate low shear stress (8-10 MPa) accommodated by quartz with minimal variations across the structure.

5. Discussion

Sheath folds are examples of complex folding mainly related to non-coaxial shearing (Oriolo et al., 2022), with hinge lines nucleating nearly orthogonal to the shear direction and tending to rotate towards the latter during progressive shearing (e.g., Carreras et al., 1977; Cobbold and Quinquis, 1980; Carreras et al., 2005; Alsop and Carreras, 2007; Schulz et al., 2008; Carreras and Druguet, 2019). In general, the formation of sheath folds is influenced by the mechanical properties of the rocks involved, such as their strength, ductility, and orientation with respect to the direction of stress (Ramsay and Huber, 1983). Various factors influence the formation of sheath folds, including the mechanical properties of the rock matrix, the orientation and location of any inclusions, and the direction and intensity of the applied stresses (Alsop and Holdsworth, 2007). For example, in areas of high strain, rocks with different mechanical properties can be subjected to different amounts of deformation and strain. This can lead to the formation of sheath folds, where more competent layers form the sheath and less competent layers form the core (Davis and Reynolds, 1996). Alternatively, if rocks are subjected to compressive stresses that are not aligned with their orientation, they may buckle and fold, leading to the development of sheath folds (Passchier and Trouw, 2005). The formation of sheath folds can also be influenced by the presence of pre-existing structures, such as faults, joints, or foliations. In these cases, the deformation may be concentrated along these features, leading to the formation of sheath folds that follow the orientation of the pre-existing structures (Ramsay and Huber, 1983).

5.1. CPO fabrics within sheath folds

The sheath fold sample was collected from the Moine Nappe between the Ben Hope Thrust (BHT) and overlying Naver Thrust (NT) in a tectonic setting marked by NW-directed tectonic transport that developed eye-type fold geometries at various scales (Holdsworth, 1989; Alsop and Holdsworth, 2004; Thigpen et al., 2013; Fig. 1). The BHT can be recognized by the juxtaposition of Lewisianoid basement inliers and amphibolite thrust to the west over psammites within a retrogressed simple shear dominated mylonite zone ~20 m thick (Holdsworth, 1989; Holdsworth and Grant, 1990; Holdsworth et al., 2001; Thigpen et al. 2013; Graziani et al, 2021). The tectonic framework of the sample site, between two major thrusts (BHT and NT, Fig. 15a), strongly influenced the CPO fabric. Understanding the CPO fabric of minerals can provide valuable insights into the deformation processes and strain distribution within the folded rocks.

The microstructural data suggests a minimal variation in deformation paths within the analyzed volume of the sheath fold. The main CPO findings are the quite consistent top-to-SE shear sense (i.e., towards the closure of the synformal sheath) in all portions of the fold irrespective of position along the three axes X, Y and Z. This sense of shear is clearly detectable from pole figures of quartz c-axis patterns (Figs. 7-10), and also corroborated by ND quartz textural findings (Figs. 12-13), suggesting minimal flow variations developed in different structural positions within the sheath fold.

For the Scandian orogenic wedge of NW Scotland, top-to the NW microstructural/crystal fabric indicators are generally recorded close to thrust sheet boundaries suggesting that either i) the rate of over-thrusting was greater than the rate of transport-parallel extrusion (Holdsworth, 1989) or, ii) that over-thrusting outlasted and overprinted the effects of transport-parallel extrusion (see Fig.13 c by Thigpen et al., 2013). A quartz c-axis pattern nearly identical to the bulk deformation fabric reported here (Fig. 9a and inset of Fig. 15a) has been published by Holdsworth and Grant (1990) for a sample collected in the proximity of the Ben Hope Thrust near the Kyle of Tongue, suggesting a comparable top-to-ESE shear sense. Similar motions, in the opposite sense to the top to the NW regional thrusts, have also been recently reported by Law et al. (2021) in an area south from the study area in the hanging wall of the Sgurr Beag Thrust, where both microstructures and quartz c-axis fabric indicate pervasive top down to the ESE-shearing. These authors explained these apparently conflicting observations with respect to the regional NW-directed tectonic transport as due to reactivation of the original thrust which was overprinted by pervasive normal sense shearing of the hanging wall and footwall rocks while they remained at close to peak temperatures.

There are a number of hypotheses that may be considered to help explain the mineral CPO outcomes in this study described in the following sections.

5.1.1. The CPO fabric is associated with passive sheath folding

In this model, the CPO is associated with the early formation of sheath folds and suggests passive (F3) folding with a constant sense of shear around the fold and across its axial surface. However, a major issue is that the CPO fabric records a top-to-SE shear direction i.e. top-to-the SE closure direction of the synformal sheath fold (Fig. 15), which is opposite to the regional (NW-directed) thrusting. The CPO fabric is therefore not in agreement with passive sheath folding created during NW-directed shear.

Furthermore, Alsop and Holdsworth's (2012) analysis of the case study fold reveals several mesoscopic features such as lineation traces wrapping the external folded surface to form "U" shaped star-burst patterns, elliptical shapes and thickness of marker layers all consistent with an active fold opening in the (NW-directed) transport direction (Alsop and Holdsworth, 2012). These authors analysis shows that axial surfaces are curvi-planar and have a consistent sense of obliquity relative to the Z axis with angles varying both in cross sections of the sheath as well as along its length. The consistent obliquity of axial planes relative to the foliation (Sn) may result in Sn transecting the sheath fold hinge, explaining why the intersection lineations "wrap" obliquely around the fold hinge. In summary, the CPO fabric analysis indicates SE-directed shear and this is not consistent with passive sheath folding created during NW-directed thrusting.

5.1.2. The CPO fabric is folded around transport-parallel hinges.

In this scenario, fold hinges that are developed parallel to transport may fold earlier kinematic indicators including CPO fabrics. The effect of folding around transport-parallel hinges is to create an apparent reversal in shear sense, although folds in general should be used with caution to determine shear sense (e.g., Krabbendam and Leslie, 1996). In the present study, top to the NW shear sense preserved on the upper limb of a transport-parallel fold could therefore be folded around the hinge to create apparent top to the SE shear on the lower fold limb. Within the study area, the fold hinges are generally parallel or sub-parallel to the NW-directed transport marked by the mineral lineation, resulting in the large-scale sheath folds as displayed by the Borgie Inlier that overlies the case study fold (Fig. 1b, Alsop and Holdsworth 2004). However, preservation of the top to the SE CPO fabrics on the lower limbs of major folds would necessitate deformation to cease almost immediately following folding so as to avoid overprinting by continued top to the NW thrusting. As thrusting and folding is thought to be progressive and operating across a number of ductile thrusts in the region (e.g., Alsop et al., 1996; Strachan et al., 2020), we consider it unlikely for thrusting to immediately cease following folding and therefore discount this model.

5.1.3. The CPO fabric post-dates the creation of the sheath fold.

In this model, the CPO is related to a late phase of crystal-plastic deformation that occurred after the formation of the sheath fold and almost completely obliterated the previous fabric associated with the sheath fold phase. The CPO therefore only records the last part of the tectono-thermal evolution and may be a more realistic model since the generally low CPO intensity of the minerals found in the sheath fold could indicate a response to a late deformation phase rather than being attributable to the initial formation of the fold.

5.1.4. Further considerations

Alsop and Holdsworth (2012) recorded culmination points from adjacent folded surfaces that are systematically offset towards the SW (right when viewed down plunge from above) and this may also provide further evidence of a shear phase postdating the fold formation. It is worth noting that the kinematic vorticity axis (CVA) reconstructed here (see Fig. 10) is not resting on the XY plane of the sheath fold as one could expect in a dominant simple shear system (Piette-Lauzière et al., 2020). This can also be explained by the systematic asymmetry of the sheath culminations with respect to the mineral lineation (Alsop and Holdsworth,2012).

Our estimates of P-T values inferred from OA measurements are consistent with Thigpen et al. (2013) and also correspond with recent estimates by Strachan et al. (2020) who note that sheath fold geometries are locally common on all scales. Within the Moine Nappe, the widespread parallelism of hornblende with L2 in mafic rocks implies that D2 was accompanied by at least low amphibolite facies metamorphism, consistent with local occurrences of syn- to post-D2 staurolite, kyanite and sillimanite. The OA data measured in this study (Table S2), which can be attributed to the amphibolite facies condition, are therefore related to deformation developed close to peak thermal conditions. This further supports the interpretation that the CPO fabric represents a deformation of the pre-existing fold with recrystallization of the quartz domains only recording this final phase.

In summary, we believe that quartz c-axis patterns of the studied sheath fold have essentially recorded one tectonic phase that has obliterated previous fabrics, such as those developed during Scandian thrusting, resulting in the development of tight-to-isoclinal F2 folds (Thigpen et al. 2013). The D2 generated a pervasive sub-horizontal foliation (S2 or Sn) and a pronounced mineral stretching lineation (L2 or Ln) interpreted to lie sub-parallel to the direction of Scandian thrust transport (Strachan et al., 2002, 2010; Law and Johnson, 2010 and references therein), evolving in the late stages of progressive deformation to a sheath folding phase (F3 folds).

Our findings are also consistent with the model of vertical ductile thinning proposed by Thigpen et al. (2013), which implies a coeval component of transport-parallel extrusion of material towards the NW (i.e. the syn-orogenic topographic surface) driven by transport-parallel stretching (top-to-SE) resulting from a vertical component of pure shear shortening (orogenic wedge loading).

5.2. Deformation patterns within sheath folds

It has long been recognized that bed-subparallel detachments may form around sheath fold closure from a km-scale (e.g., Alsop 1992, 1994; Searle and Alsop, 2007) to a metre scale (Alsop and Holdsworth, 2012). The location of detachments may be partially controlled by original lithological heterogeneity which influenced deformation in the early more ‘active’ stages of folding. As folding of the competent layers develops, they may locally truncate adjacent beds leading to low-angle detachments observed around sheath fold noses (e.g., Alsop, 1994; Searle and Alsop, 2007; Alsop and Holdsworth, 2012). Such folds and associated detachments are subsequently accentuated during more passive deformation associated with flow and amplification of sheath folds.

We suggest that where sheath folds comprise ~~more competent and weaker~~ inter-layered units, then ductile flexural slip may occur as a result of the differential deformation between the more competent and the weaker beds (Fig. 15c). As the deformation progresses, the weaker layers and interfaces undergo flexural deformation, with slip concentrating along these weaker layers to accommodate the strain. The slip can take place parallel or oblique to the fold axis, depending on the orientation of the stress field and the mechanical anisotropy of the rock layers. The resulting sheath folds exhibit characteristic tongue shapes, with parallel-sided limbs marked by slip along the weaker layers or interfaces. The sense of slip results in 'extrusion' of the core of the fold that will correspond with a top to the SE shear on the lower fold limb and top to the NW shear on the upper limb of a synform that closes to the SE (Fig. 15c).

In detail, while there is no evidence for a reversal in CPO shear sense across the axial surface of the sample fold that the model would require, the regional position of the sample site in a synform that underlies the large-scale Borgie sheath fold broadly corresponds to this scenario (Figs. 1, 15a, c). We also note that in this study we only investigated the apical part of the overall sheath fold (slices 15, 16, 17, 18; see Fig. 3) where the extruding core is only partially preserved (i.e. marker layer 6). We have therefore avoided complexities due to doubling of fold cores (double eye-type pattern) in the opening part of the fold, as well as the occurrence of internal detachment surfaces that disarticulate the enveloping concentric layers near the lower limb. This may explain the low inhomogeneity within the mineral CPO fabric, and this study can thus be considered a first attempt to characterize the relatively simple apex of sheath fold closures.

6. Conclusion

The case study fold is considered to have formed during non-coaxial deformation associated with regional NW-directed shear (Alsop and Holdsworth, 2012). The kinematics of the fold inferred from the mineral CPO is antithetic (i.e. top-to-SE) to this general NW-directed tectonic transport of large-scale folds and vergence of the main thrusts (BHT to NT). This relationship is observed in areas of high strain rate where it is not unusual to observe secondary structures showing opposite shear directions with respect to those of the main regional structure.

The sheath fold sample was collected within the axial zone of a large-scale synform (Fig. 1c) and could therefore represent such a minor structure in which, due to a ~~ductile flexural slip~~ mechanism on the inverted limb of the fold, shear ~~directions~~ where locally opposite to the general shear ~~direction~~ that formed the main fold. Alternatively, it may reflect the local top to the SE-directed shear sense associated with a larger active sheath fold (Fig. 15c). However, the CPO results are not consistent with such a claim since they indicate a SE-directed shear.

In view of the previous detailed morphological study of the multi-layered sheath fold by Alsop and Holdsworth (2012), together with the mineral CPO measured in the present study, we can conclude that an early active folding stage of the studied sheath fold has been extensively masked and pervasively obliterated by a top-to-SE normal ~~shear sense~~. Our results suggest that even if macroscopic evidence of active folding occurs, the earlier CPO fabric has been almost completely obliterated and it reflects instead the last deformational phases showing a constant top-to the SE sense of shear which is opposite to the main NW-directed tectonic transport of major thrusts. We note that microstructural and quartz c-axis data recently reported by Law et al. (2021) from the Caledonides of northern Scotland also indicate a comparable normal-sense top down-SE shearing, probably developed at close to peak temperatures at ~420 Ma. We follow these authors to suggest that top to the SE shear may relate to the closing stages of Scandian deformation, metamorphism and cooling/exhumation.

Acknowledgments

This has been a multi-national collaboration from authors based in Europe, North America, Australia and India. The sheath fold sample was originally collected by G.I.A. in 2005, with Erasmus funding in 2018 enabling a visit to Catania leading to discussion and initiation of this project. The authors are grateful to Amarnath Dandapat for preparation of superpolished rock thin sections at the Department of Geology and Geophysics (IIT Kharagpur, India). Niloy Bhowmik is thanked for assistance with SEM-EBSD data generation in the Central Research Facility (IIT Kharagpur, India). E.F. thanks Sibio Carmelo for thin sections preparation at the University of Turin (Italy). Authors are grateful to ANSTO laboratory personnel for the preparation of specimens (funded proposals: P9835 with the title *"Sheath fold texture characterisation"*, principal scientist: E.F.; co-proposers: G.I.A. and V.L.; DB6749 with the title *"Texture analysis of rocks"*, principal scientist: V.L.; co-proposer: E.F.; DB9606 with the title *"A pilot experiment for texture characterisation in a sheath fold"*, principal scientist: E.F..; co-proposers: G.I.A. and V.L.).

Figure captions

Fig.1 – a) Geological map of the northern Scottish Highlands with sample location (modified from Alsop et al., 2021). b) Schematic cross-section (see a for location and orientation) (modified after Alsop et al., 2021). c) Detailed geological map of the study area (red star marks the sheath-fold sample location; modified from Alsop and Holdsworth, 2012).

Fig. 2 – a) Back (top right) and upper (bottom right) views of the collected sample (Alsop and Holdsworth, 2012) and sketch model (left) of the sheath fold. b) *T*he four slices (15, 16, 17, 18) where microdomains have been selected for textural analyses (marker layers 6, 7, and 11 are shown as red, green and purple lines, respectively). c) Photograph of polished surfaces of slices 15, 16, 17, and 18 used in this study (labels a and b refer to the larger downside and smaller upside faces of the same slice, respectively). d) 3D view of orthogonal sections and transversal slice 8a. e) 3D view of picked markers within all the transversal sections. f) Construction of 3D marker surfaces n°11 (see Supp. Fig. 1). Upper and lower limbs are developed separately and successively merged together. g) 3D view of all the nine modelled marker surfaces. h) 3D view (clipping view) showing the internal structure of the sheath fold (marker layers used are the same traced by Alsop and Holdsworth, 2012).

Fig. 3 – Schematic draw sketch of foliation traces (Sn) inferred from scanned thin sections (XZ plane) analyzed by means of the EBSD technique.

Fig. 4 – Overview of microstructures within the studied psammite. a) Panoramic of biotite flakes defining the main foliation as seen along YZ plane of finite strain ellipsoid (crossed-polarizer light with lambda plate). b) Irregular, lobate quartz grain boundaries (arrow), pointing dynamic recrystallization in the grain boundary migration regime for quartz (crossed-polarizer light). c) Pinning microstructure (arrow) of quartz grain boundaries on biotite (crossed-polarizer light). d) Myrmekite (arrow) growth along K-feldspar grain boundary (crossed-polarizer light). Mineral abbreviations: Bt - biotite, K-Feld - K-feldspar, Pl - plagioclase, Qz - quartz.

Fig. 5 – Example of elaborated SEM-EBSD maps (sample 16a-I; see Supplementary materials for the complete dataset). a) Phase map, showing quartz and biotite grains. b) Inverse pole figure map of quartz, showing internal

subgrains (delimited by purple lines) and Dauphiné twinning (green lines). The colours refer to the crystallographic direction oriented parallel to the lineation (X-axis of the finite strain ellipsoid of the sheath fold). c) Kernel Average Misorientation (KAM) map for quartz grains. The red gradient indicates misorientation grade among neighbour pixels. Subgrains (> 2°) are highlighted by purple lines, Dauphiné twinning by green lines. d) subset of the KAM map c).

Fig. 6 – a) Examples of quartz grain size maps of two areas representative of two different sheath fold slices. The colour-coded calibration bar indicates the radius of the grain equivalent circle (μm). b) Examples of grain size distribution histograms for representative areas of the four studied sheath fold slices (logarithmic scale for the grain size axis). c) Quartz grain size distribution histogram for the bulk sheath fold (after noise removal), showing the mean and the median grain size (logarithmic scale for the grain size axis). A.R. is the mean aspect ratio of quartz grains of the bulk sampling. See Supplementary materials for the complete dataset.

Fig. 7 – Quartz and biotite pole figures (lower hemisphere, equal area projection) of two representative areas of the sheath fold. All texture projection planes are sections oriented parallel to the XZ-plane of the finite strain ellipsoid with respect to the flattening direction of the sheath fold. Colour bar scales indicate multiples of uniform distribution of the de la Vallée Poussin Kernel function (Schaeben, 1997) with an halfwidth of 10° (Hielscher and Schaeben, 2008). Supplementary materials for the complete dataset.

Fig. 8 – Quartz c-axis pole figures (lower hemisphere, equal area projection). All texture projection planes are oriented parallel to the XZ-plane of the finite strain ellipsoid with respect to the flattening direction of the sheath fold itself. Colour bar scale (top right box) indicates multiples of uniform distribution of the de la Vallée Poussin Kernel function. When possible, the foliation plane marked by biotite (within the sheath fold) is plotted (grey dashed line) accounting mica grain shape orientation, at the microscale, and its CPO (e.g., see Fig. 5c, d for biotite CPOs).

Fig. 9 – a) Quartz and b) biotite pole figures (one point per pixel) for the sheath fold analysed areas (lower hemisphere equal area projection, projection planes are oriented parallel to the XZ plane). c) Inverse pole figure of the quartz misorientation axes for slip systems interpretation (modified after Neumann, 2000; Wheeler et al., 2001), and quartz misorientation axes plot for the bulk analysed areas (rotation axes associated with subgrain domains for threshold misorientations angles of 2°-10°; grain boundaries for threshold misorientations angles between 10°-15°). All colour bar scales indicate multiples of uniform distribution of the de la Vallée Poussin Kernel function.

Fig. 10 – a-f) Quartz pole figures (EBSD) and opening angle (OA) measured on crossed girdle patterns. g) Bulk OA. h) PT diagram showing OA results (plotted red and blue lines after Morgan and Law, 2004, and Faleiros et al., 2016, respectively).

Fig. 11 – a-d) Examples of quartz and biotite kinematic vorticity axis (CVA) plots for selected areas of the slices

of the sheath fold (see Supplementary materials for the complete dataset). **e**) CVA orientation plots for the combination of quartz and biotite orientations (bulk plot) and for the bulk analysed quartz and biotite (representative for the entire analysed volumes of the sheath fold). All pole figures are in sample coordinates: lower hemisphere equal area projection; projection planes oriented parallel to the XZ plane; reference in (e). Colour bar scales indicate multiples of uniform distribution of the de la Vallée Poussin Kernel function.

Fig. 12 – Pole figures for quartz (Qz) and biotite (Bt) textures measured by means of ND (Neutron Diffraction) technique for the 17a slice (different investigated sub-volumes are indicated).

Fig. 13 – Pole figures for quartz (Qz) and biotite (Bt) textures measured by means of ND (Neutron Diffraction) technique for the 15a slice (different investigated sub-volumes are indicated).

Fig. 14 – Neutron tomography of a sub-volume (17a-V) of slice 17a (see supplementary material for volume location): a) Orthogonal slices through the reconstructed volume of the samples with location of the cropping planes indicated in the three-dimensional model in the top-left corner (XZ, XY, YZ planes are in red, green, and blue colour, respectively). b) Three-dimensional distribution of mineral phases shown in different directions- one perspective and three orthogonal ones. Phases are rendered based on the colour code used to define the thresholding values adopted for the segmentation in c) the histogram of the frequency distribution of the neutron attenuation coefficients. The phases attributed to each segmented region in the histogram and the corresponding volume fraction percentage are reported in d).

Fig. 15 – a) Block diagram showing the Scandian orogenic wedge of NW Scotland (not to scale) top right insets: stereoplot with poles to mylonitic foliation (Sn - marker layer 11) reconstructed by the 3D model of the sheath fold (Move software; n. 5827 surfaces were sampled) and bulk pole figure of quartz c-axes orientation (Qz grains n. 6846). b) Mesoscopic 3D sketches of an active sheath fold (after Alsop and Holdsworth, 2012).; c) (top) schematic diagrams of a simple ductile thrust model to explain the evolution of the Caledonian structures in the Moine Nappe (modified after Holdsworth, 1989) with lateral layer parallel extrusion and an orogenic wedge loading compatible with a sub-vertical sigma 1 and (bottom) position of the studied mesoscopic sheath fold showing a top to the SE shear sense in the lower hinge of a regional-scale synformal fold.

Tables

Table 1 – sample number, differential stress obtained by the subgrains and grain size method, and CPO strength highlighting J-Index and M-Index.

Table 1.

Sample	N. pixels (Qz)	N. grains (Qz)	N. pixels (Bt)	N. grains (Bt)	J-Index	M-Index	Shear stress (grain size) (MPa)	Shear stress (subgrains) (MPa)
15A II	97017	708	727	42	1.64	0.02	28.6	9.8
15A IV	79341	623	1769	71	1.72	0.03	28.3	8.2
15A V	95673	585	1122	55	1.63	0.02	27.2	8.3
15A IX	109636	728	1648	83	1.72	0.03	29.7	11.8
16A I	80150	694	3261	156	1.50	0.02	29.8	10.2
16A II	90220	550	2116	105	1.71	0.03	29.1	11.0
16A IV	98280	727	1378	69	1.64	0.02	32.5	8.4
17A I	82508	558	1788	78	1.57	0.02	25.8	10.0
17A II	97230	631	1731	83	1.81	0.03	30.2	9.3
17A III	86617	502	520	33	1.66	0.02	28.2	10.0
18A II	80995	540	2511	115	1.55	0.01	28.3	8.7
Total	Qz grains	Qz pixel	Bt grains	Bt pixel				
volume	6846	997667	890	18571				

Table 1. Summary of the main results for quartz (Qz) and biotite (Bt). The number of pixels defining the analysed number of grains is reported. The CPOs strengths, expressed by the J-Index (or "texture index", Bunge, 1982) and the M-Index (Skemer et al., 2005), are reported only for quartz. The shear stress (recalculated from the grain size, Cross et al 2017, and the subgrains, Goddard et al., 2020, with a subgrain threshold of 1°) indicates the differential stress accommodated by quartz during dynamic recrystallization.

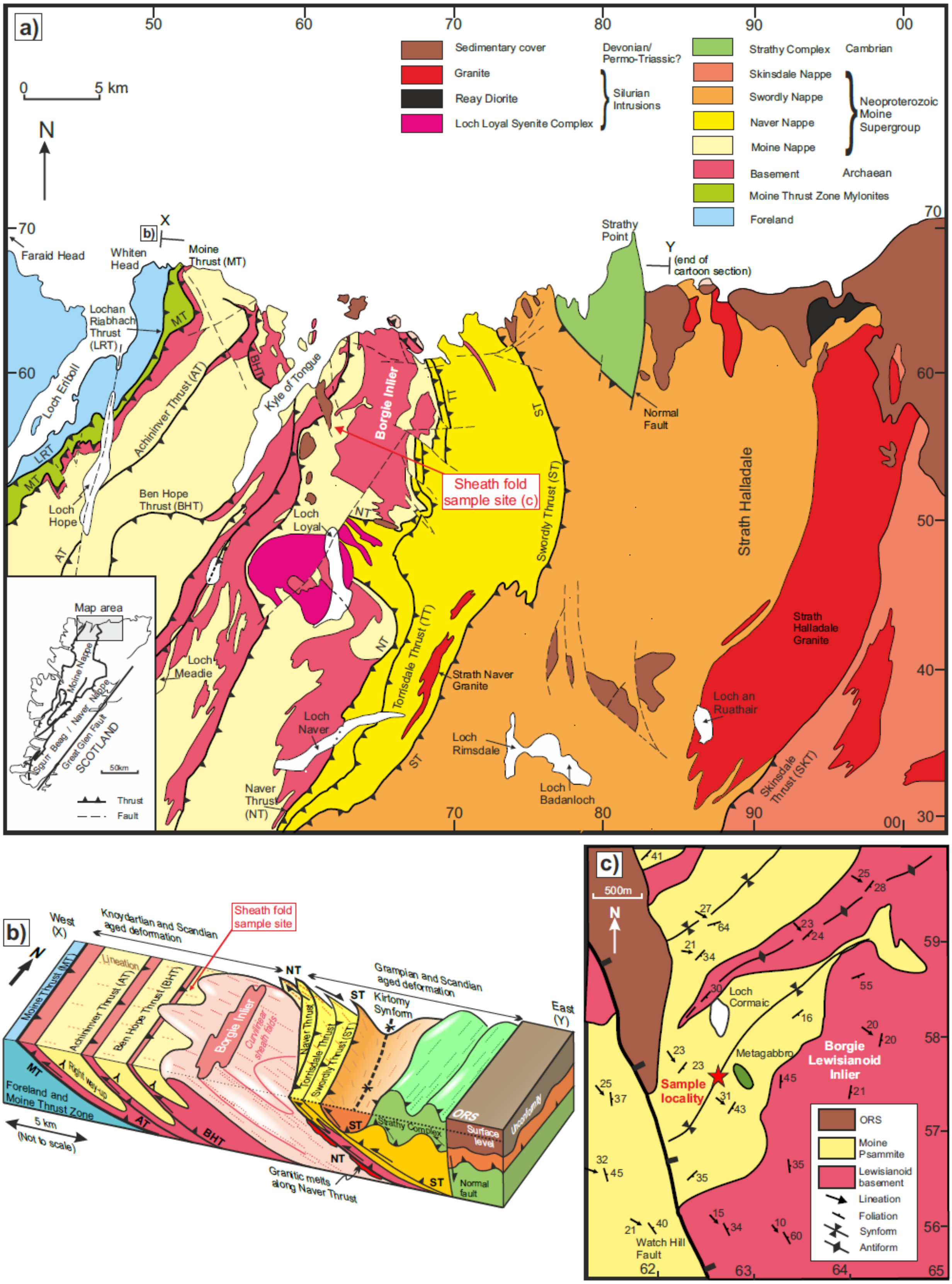
a)
Sedimentary cover
Granite
Reay Diorite
Loch Loyal Syenite Complex
Devonian/
Permo-Triassic?
Silurian
Intrusions
Strathy Complex
Cambrian
Skinsdale Nappe
Swordly Nappe
Naver Nappe
Moine Nappe
Neoproterozoic
Moine
Supergroup
Basement
Archaean
Moine Thrust Zone Mylonites
Foreland
0
5 km
N
Faraid Head
Whiten
Head
Moine
Thrust (MT)
Lochan
Riabhach
Thrust
(LRT)
Loch Eriboll
LRT
MT
Achininver Thrust (AT)
BHT
Kyle of Tongue
Borgie Inlier
Sheath fold
sample site (c)
Strathy
Point
Y
(end of
cartoon section)
Normal
Fault
Strath Halladale
Loch
Hope
Ben Hope
Thrust (BHT)
Loch
Loyal
NT
Swordly Thrust (ST)
Map area
Moine Nappe
Naver Nappe
Sgurr Beag / Naver
Great Glen Fault
SCOTLAND
50km
Thrust
Fault
Loch
Meadie
Loch
Naver
Naver
Thrust
(NT)
Torrisdale Thrust (TT)
Strath Naver
Granite
Loch
Rimsdale
Loch
Badanloch
Strath
Halladale
Granite
Loch an
Ruathair
Skinsdale
Thrust (SKT)
b)
West
(X)
Knoydartian and Scandian
aged deformation
Sheath fold
sample site
Grampian and Scandian
aged deformation
East
(Y)
Moine Thrust (MT)
Achininver Thrust (AT)
Ben Hope Thrust (BHT)
Lineation
Borgie Inlier
Curvilinear sheath folds
Naver Thrust
Torrisdale Thrust
Swordly Thrust (ST)
Kirtomy
Synform
Strathy Complex
ORS
Unconformity
Surface
level
Normal
fault
Foreland and
Moine Thrust Zone
Right way-up
Granitic melts
along Naver Thrust
5 km
(Not to scale)
c)
500m
N
Loch
Cormaic
Metagabbro
Borgie
Lewisianoid
Inlier
Sample
locality
Watch Hill
Fault
ORS
Moine
Psammite
Lewisianoid
basement
Lineation
Foliation
Synform
Antiform

Fig.1

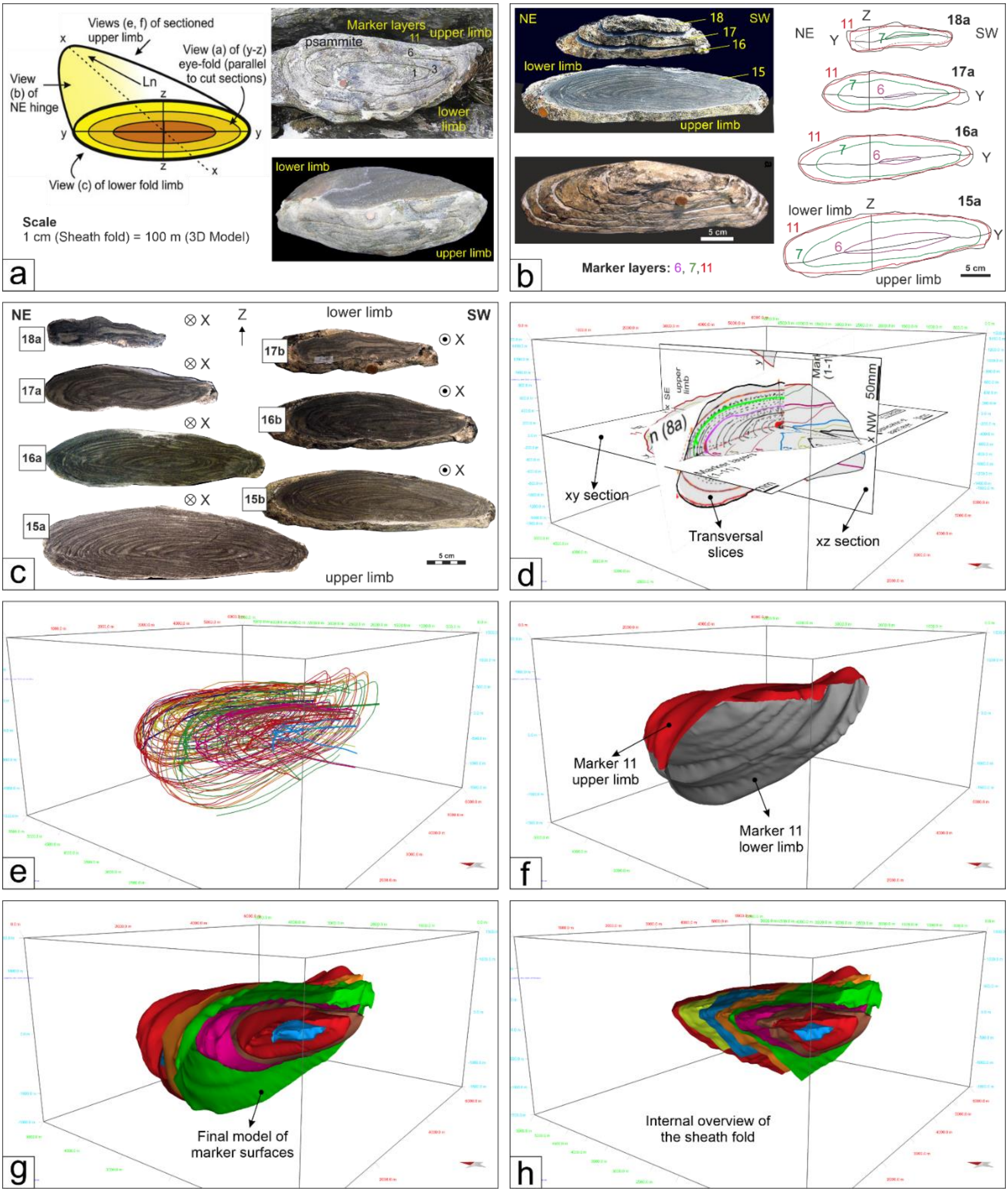
Views (e, f) of sectioned upper limb
View (a) of (y-z) eye-fold (parallel to cut sections)
View (b) of NE hinge
View (c) of lower fold limb
Ln
Scale
1 cm (Sheath fold) = 100 m (3D Model)
Marker layers
psammite
upper limb
lower limb
NE
SW
lower limb
upper limb
5 cm
Marker layers: 6, 7, 11
18a
17a
16a
15a
lower limb
upper limb
5 cm
NE
SW
18a
17a
16a
15a
17b
16b
15b
lower limb
upper limb
5 cm
xy section
Transversal slices
xz section
50mm
Marker 11 upper limb
Marker 11 lower limb
Final model of marker surfaces
Internal overview of the sheath fold
a
b
c
d
e
f
g
h

Fig. 2.

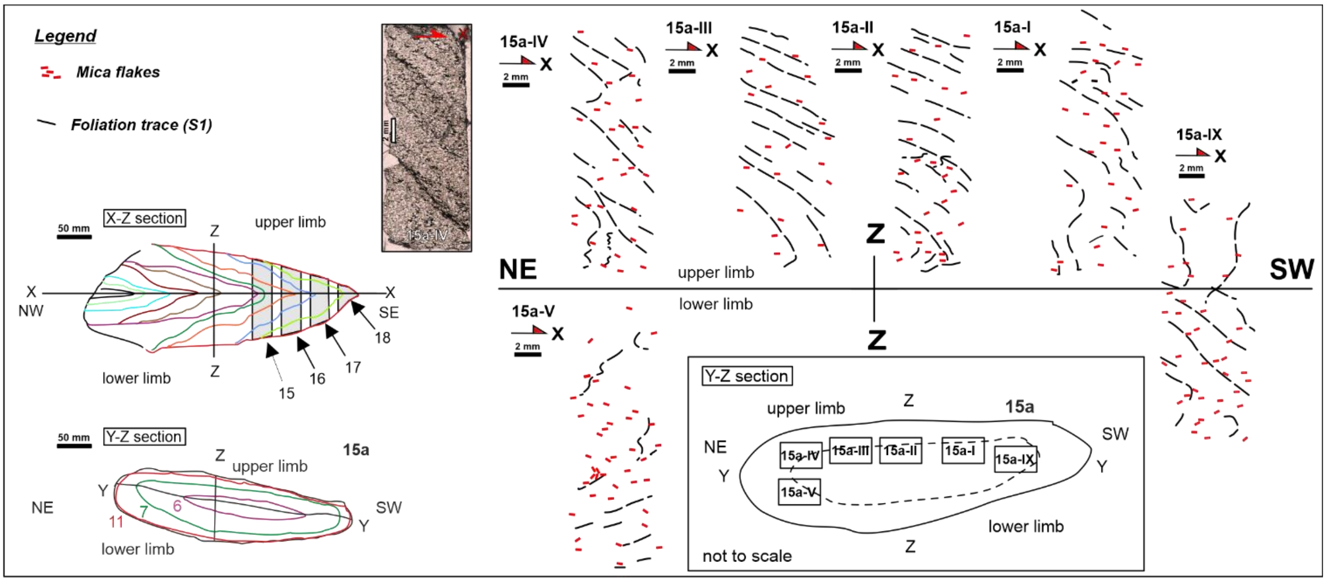
Legend
Mica flakes
Foliation trace (S1)
50 mm
X-Z section
upper limb
lower limb
NW
SE
15
16
17
18
Y-Z section
15a
NE
SW
11
7
6
15a-IV
15a-III
15a-II
15a-I
15a-IX
15a-V
2 mm
NE
SW
upper limb
lower limb
Y-Z section
not to scale

Fig. 3

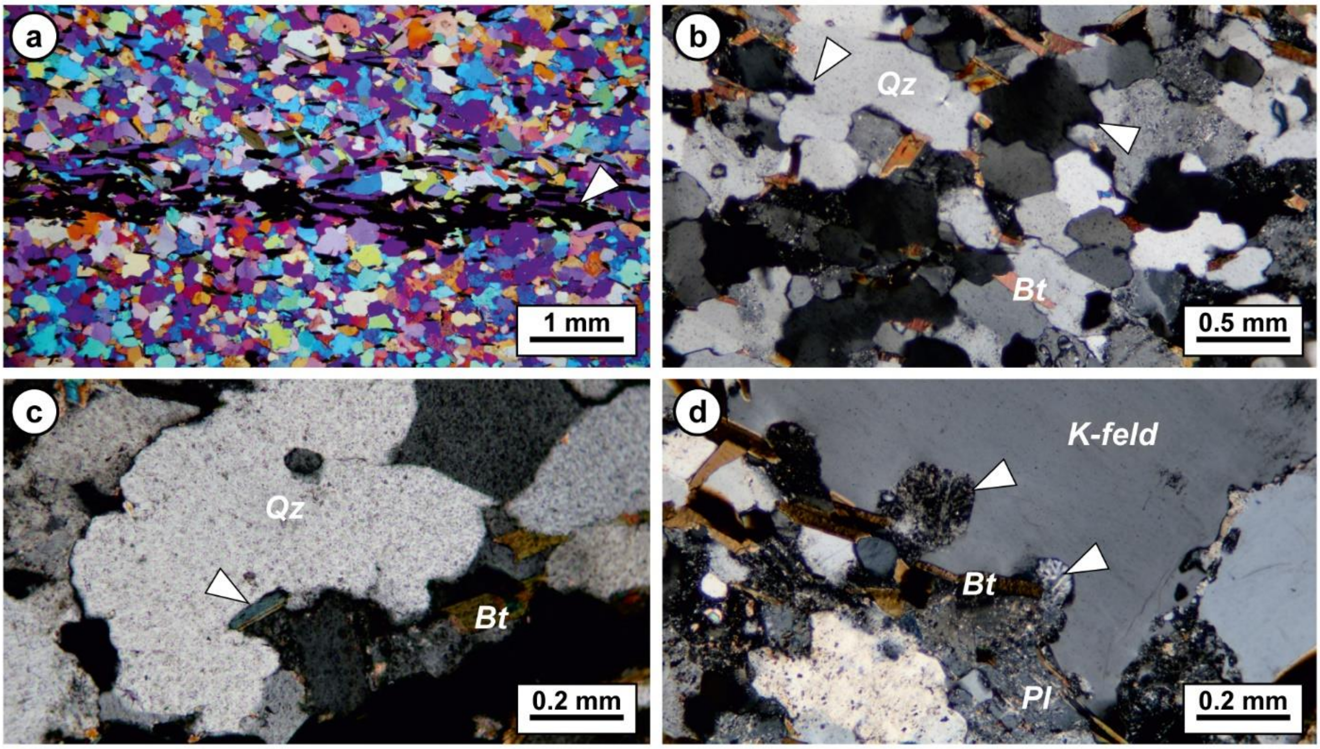
a
1 mm
b
Qz
Bt
0.5 mm
c
Qz
Bt
0.2 mm
d
K-feld
Bt
Pl
0.2 mm

Fig. 4

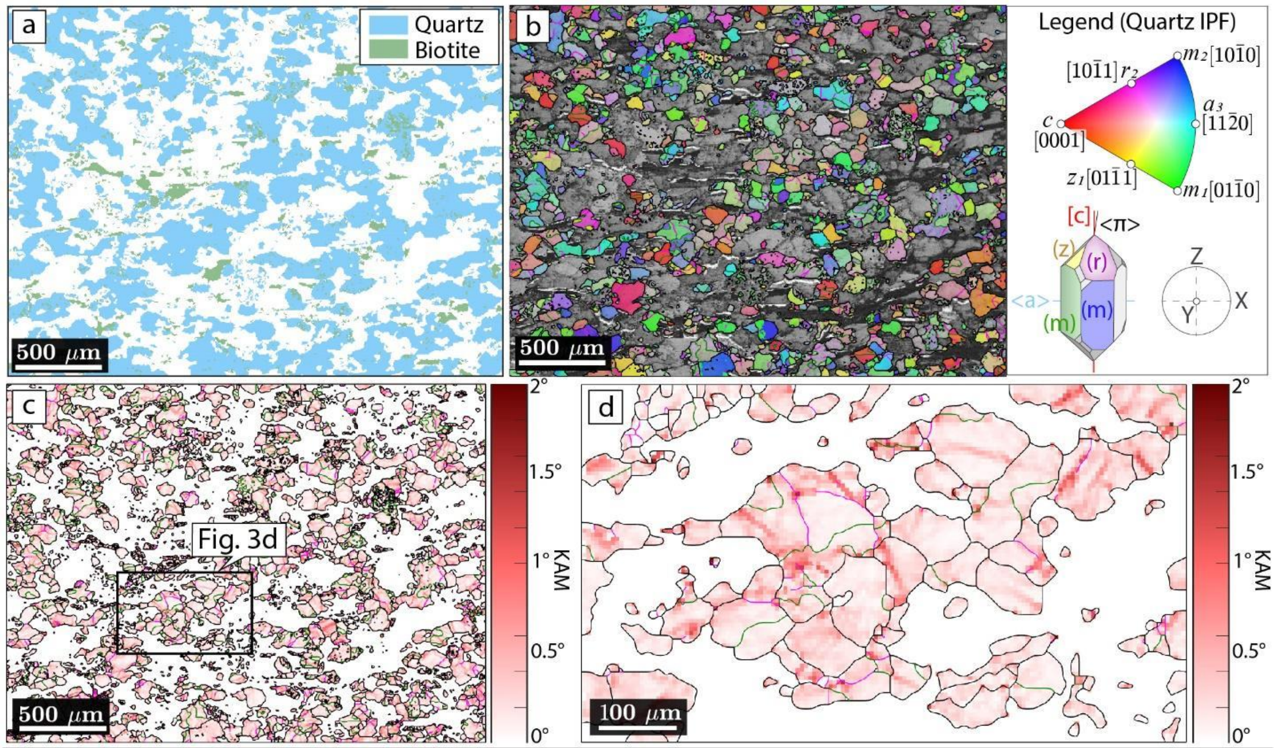
a
Quartz
Biotite
500 μm
b
500 μm
Legend (Quartz IPF)
c
[0001]
[10$\bar{1}$1] r_2
m_2[10$\bar{1}$0]
a_3
[11$\bar{2}$0]
z_1[01$\bar{1}$1]
m_1[01$\bar{1}$0]
[c]
<π>
(z)
(r)
<a>
(m)
(m)
Z
X
Y
c
Fig. 3d
500 μm
2°
1.5°
1°
0.5°
0°
KAM
d
100 μm
2°
1.5°
1°
0.5°
0°
KAM

Fig. 5

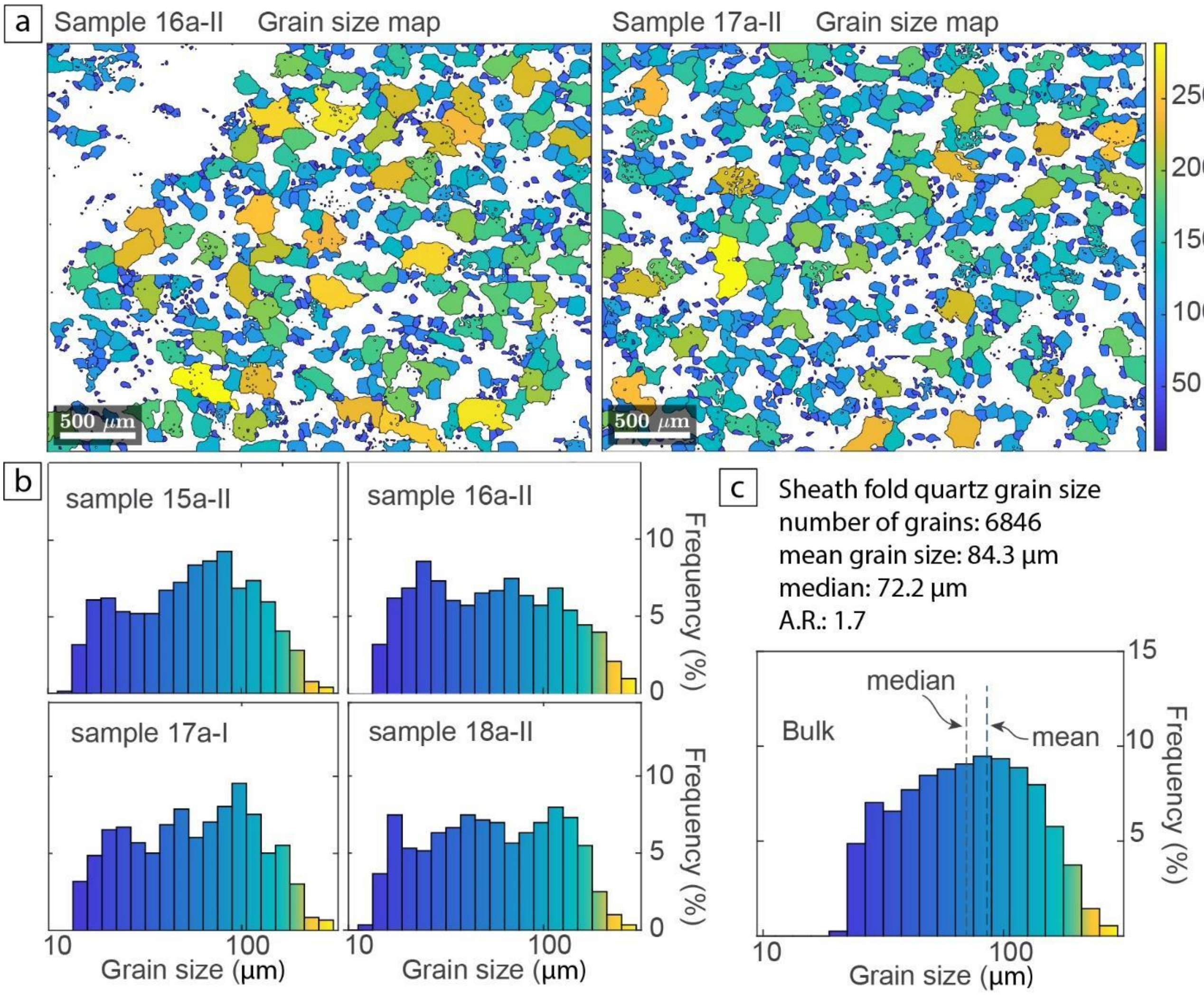
a
Sample 16a-II Grain size map
Sample 17a-II Grain size map
500 μm
500 μm
250
200
150
100
50
b
sample 15a-II
sample 16a-II
sample 17a-I
sample 18a-II
Frequency (%)
10
5
0
Grain size (μm)
10
100
c
Sheath fold quartz grain size
number of grains: 6846
mean grain size: 84.3 μm
median: 72.2 μm
A.R.: 1.7
Bulk
median
mean
15
10
5
Frequency (%)
Grain size (μm)

Fig. 6

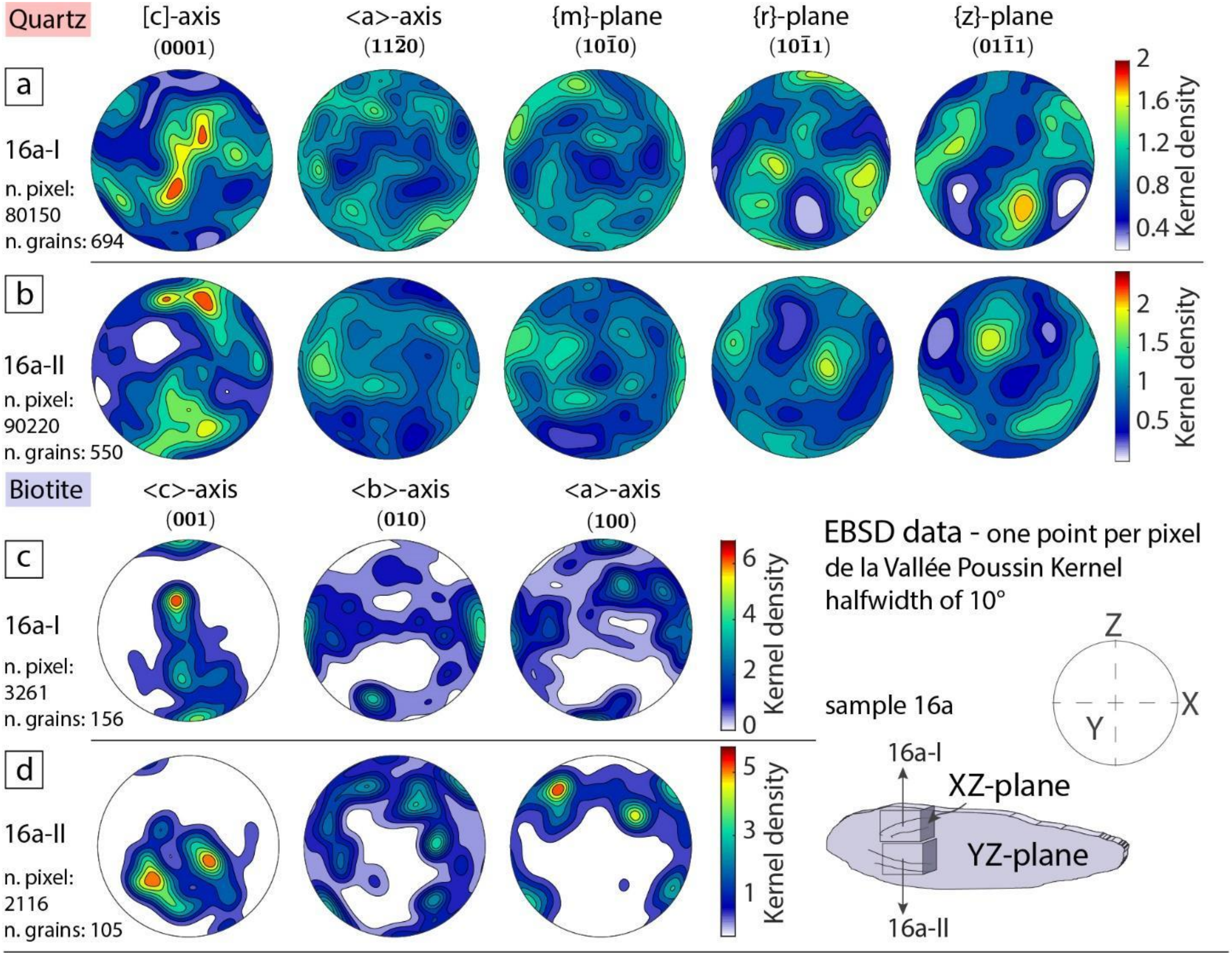

Quartz
[c]-axis
(0001)
<a>-axis
(11$\bar{2}$0)
{m}-plane
(10$\bar{1}$0)
{r}-plane
(10$\bar{1}$1)
{z}-plane
(01$\bar{1}$1)
a
16a-I
n. pixel:
80150
n. grains: 694
b
16a-II
n. pixel:
90220
n. grains: 550
Kernel density
Biotite
<c>-axis
(001)
<b>-axis
(010)
<a>-axis
(100)
c
16a-I
n. pixel:
3261
n. grains: 156
d
16a-II
n. pixel:
2116
n. grains: 105
Kernel density
EBSD data - one point per pixel
de la Vallée Poussin Kernel
halfwidth of 10°
Z
X
Y
sample 16a
16a-I
XZ-plane
YZ-plane
16a-II

Fig. 7

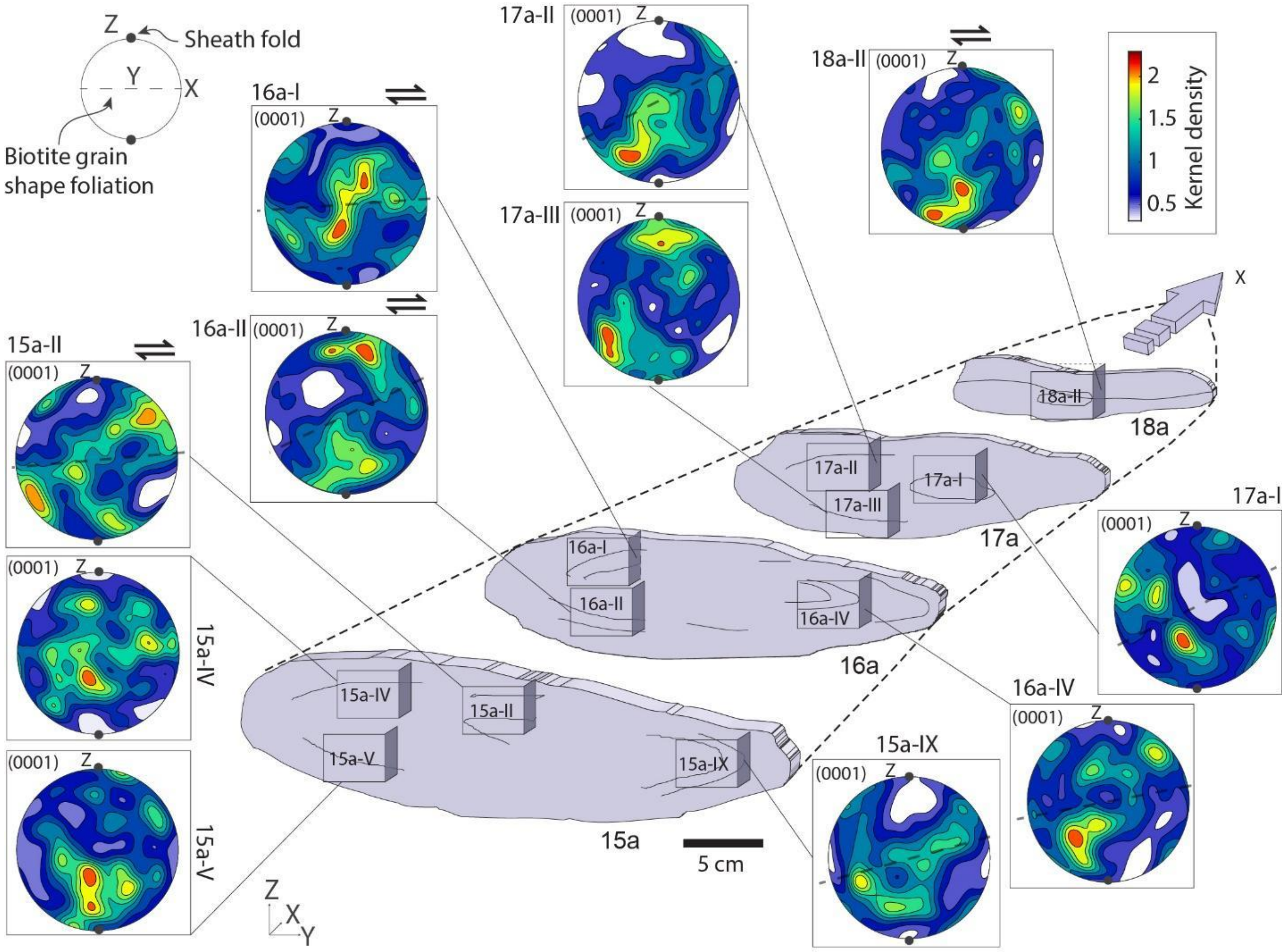

Z
Sheath fold
Y
X
Biotite grain shape foliation
16a-I
(0001)
16a-II
17a-II
17a-III
18a-II
Kernel density
2
1.5
1
0.5
15a-II
15a-IV
15a-V
17a-I
16a-IV
15a-IX
18a
17a
16a
15a
5 cm

Fig. 8

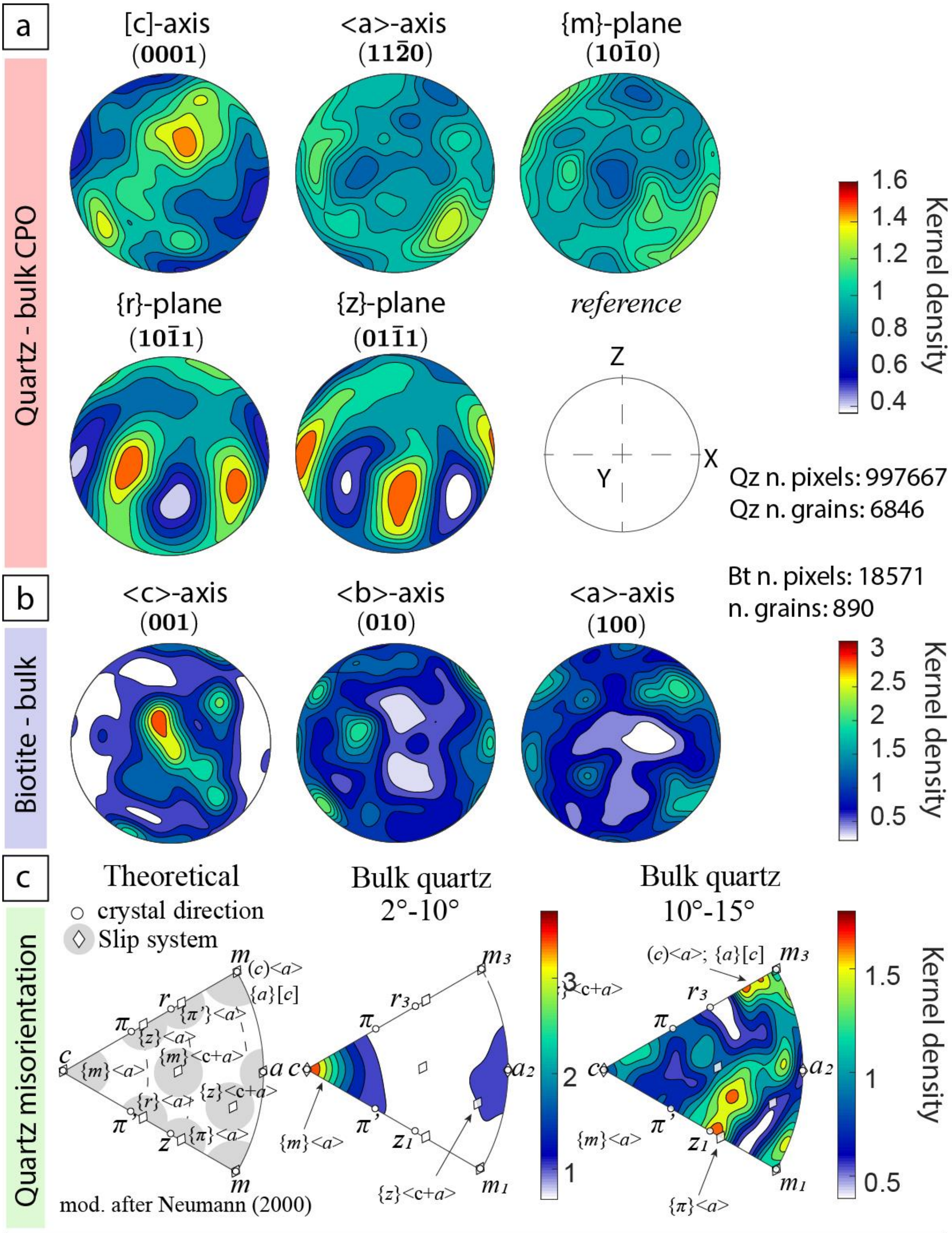

a
[c]-axis
(0001)
<a>-axis
(11$\bar{2}$0)
{m}-plane
(10$\bar{1}$0)
{r}-plane
(10$\bar{1}$1)
{z}-plane
(01$\bar{1}$1)
reference
Z
X
Y
Quartz - bulk CPO
1.6
1.4
1.2
1
0.8
0.6
0.4
Kernel density
Qz n. pixels: 997667
Qz n. grains: 6846
Bt n. pixels: 18571
n. grains: 890
b
<c>-axis
(001)
<b>-axis
(010)
<a>-axis
(100)
Biotite - bulk
3
2.5
2
1.5
1
0.5
Kernel density
c
Quartz misorientation
Theoretical
crystal direction
Slip system
mod. after Neumann (2000)
Bulk quartz
2°-10°
Bulk quartz
10°-15°
(c)<a>
{a}[c]
{π'}<a>
{z}<a>
{m}<c+a>
{m}<a>
{r}<a>
{z}<c+a>
{π}<a>
(c)<a>; {a}[c]
{m}<a>
{z}<c+a>
{π}<a>
Kernel density
1.5
1
0.5

Fig. 9

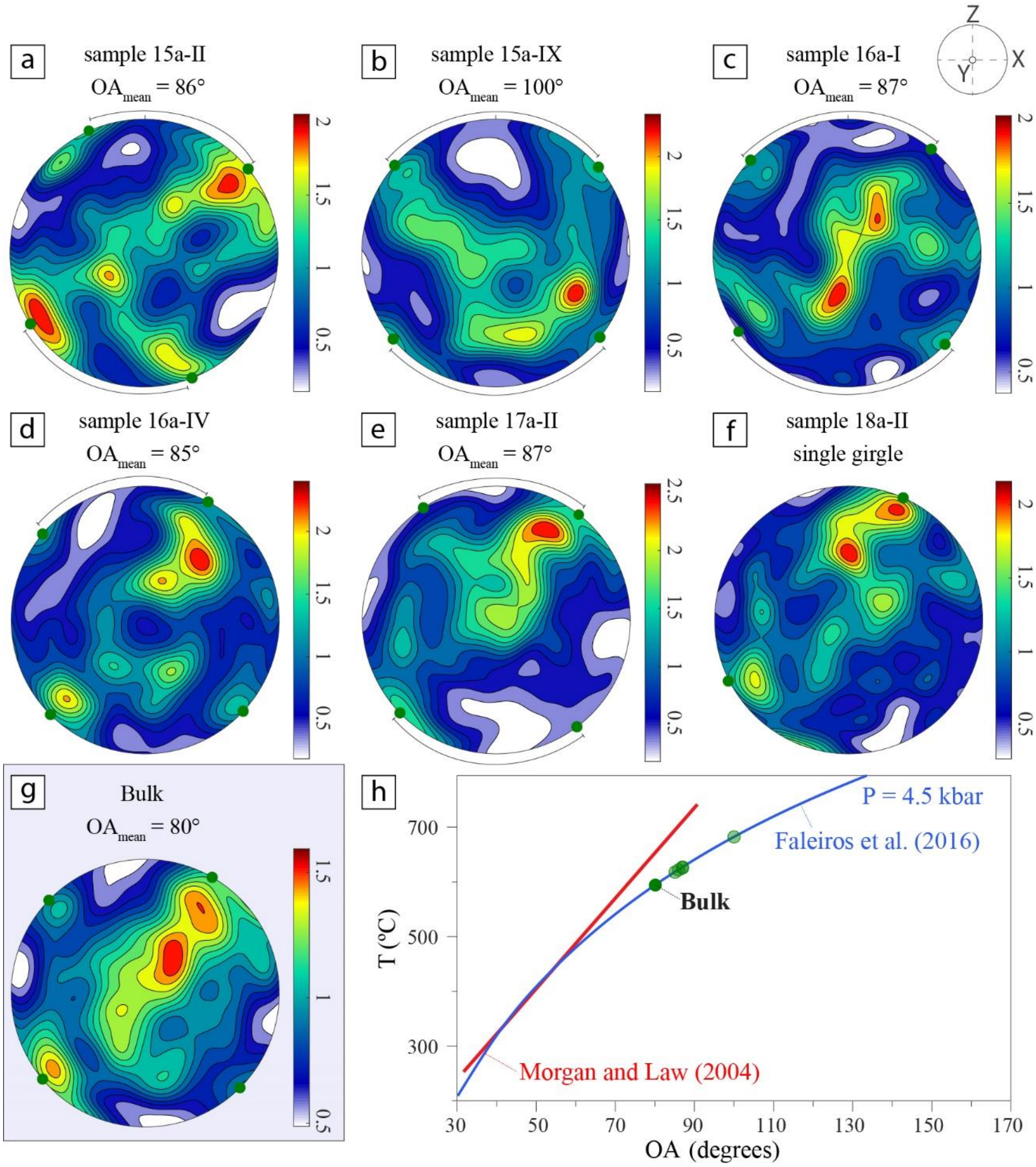
a
sample 15a-II
OA_{mean} = 86°
b
sample 15a-IX
OA_{mean} = 100°
c
sample 16a-I
OA_{mean} = 87°
Z
X
Y
d
sample 16a-IV
OA_{mean} = 85°
e
sample 17a-II
OA_{mean} = 87°
f
sample 18a-II
single girgle
g
Bulk
OA_{mean} = 80°
h
P = 4.5 kbar
Faleiros et al. (2016)
Bulk
Morgan and Law (2004)
T (°C)
OA (degrees)

Fig. 10

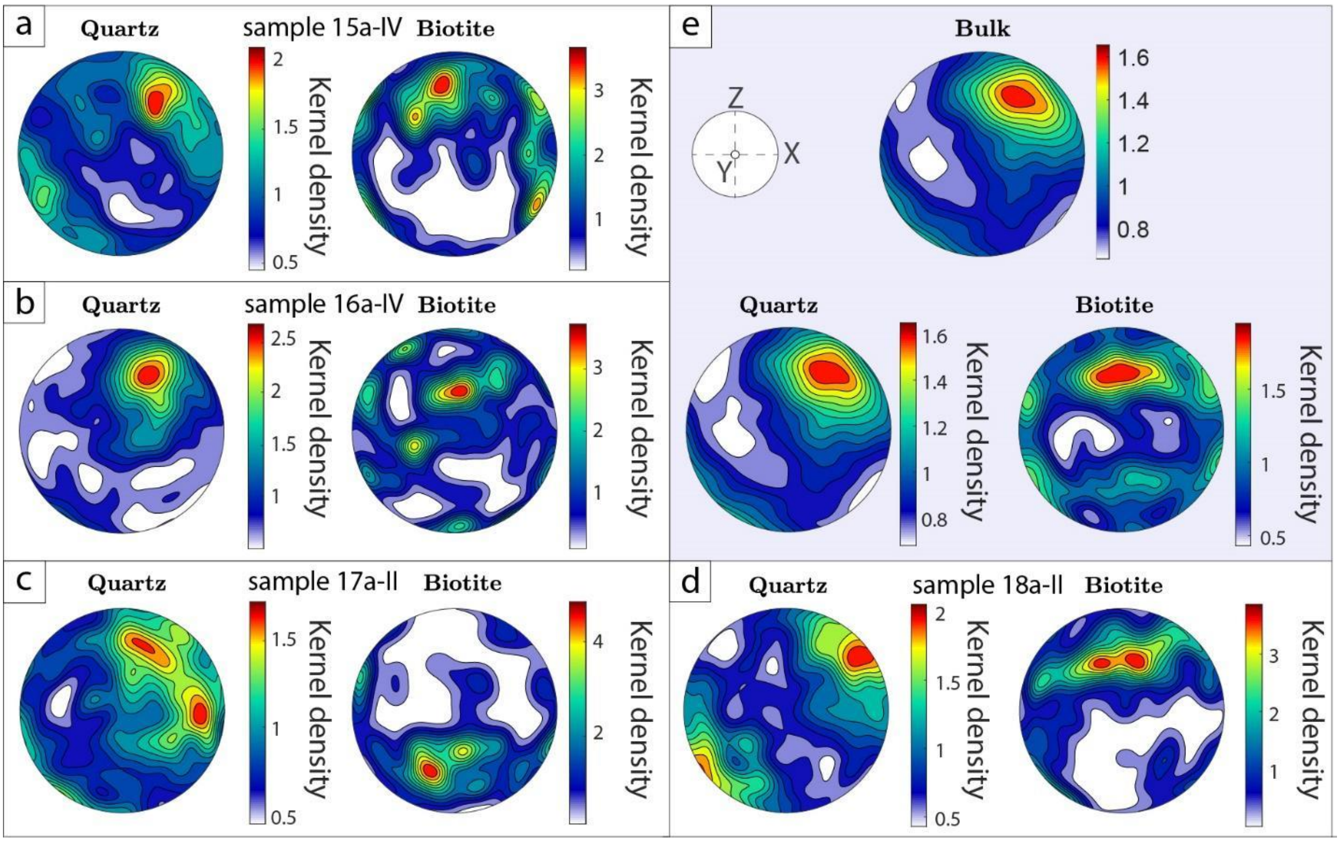

a
Quartz
sample 15a-IV
Biotite
Kernel density
b
Quartz
sample 16a-IV
Biotite
Kernel density
c
Quartz
sample 17a-II
Biotite
Kernel density
d
Quartz
sample 18a-II
Biotite
Kernel density
e
Bulk
Z
X
Y
Quartz
Biotite
Kernel density

Fig. 11

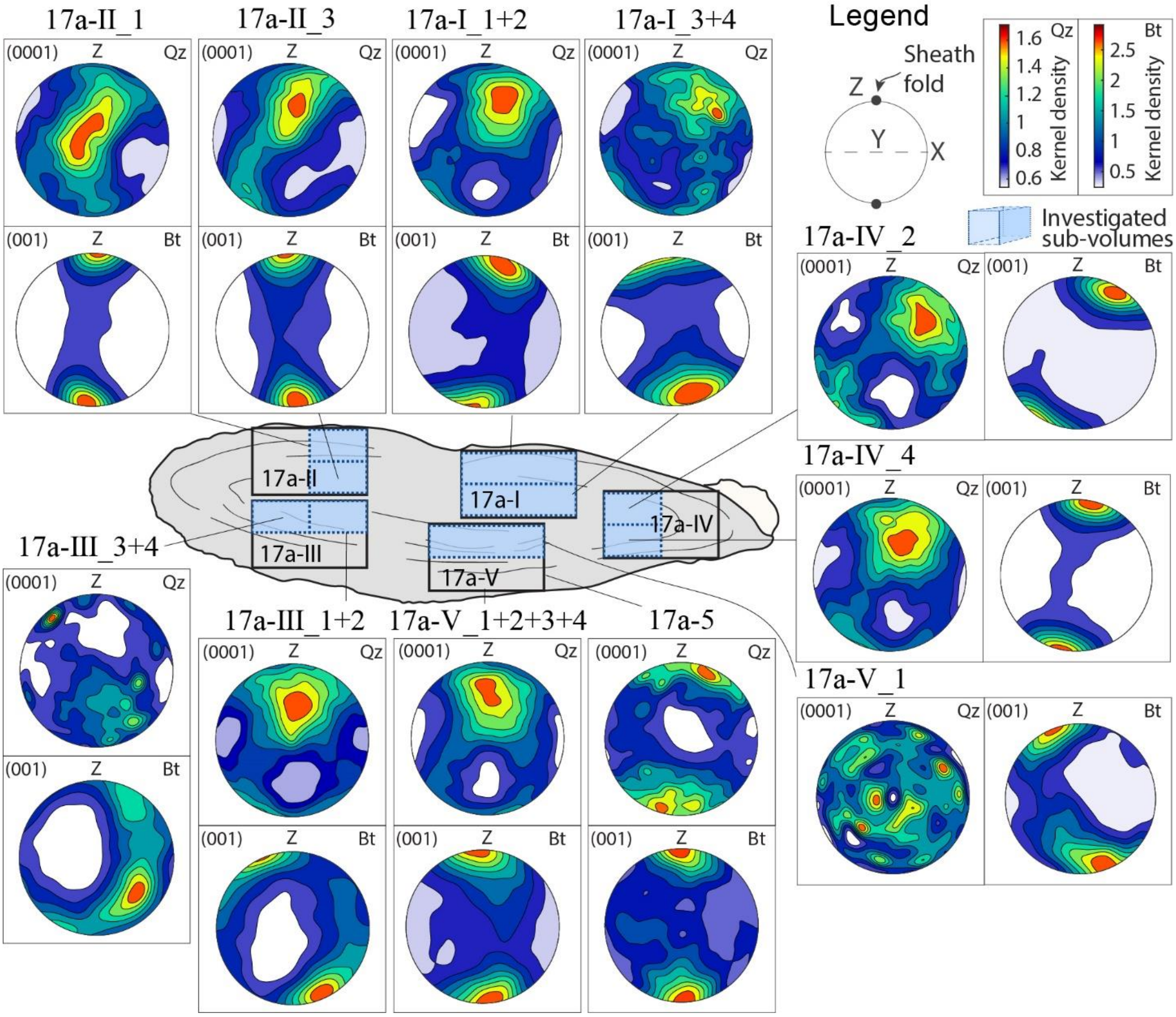
17a-II_1
17a-II_3
17a-I_1+2
17a-I_3+4
Legend
Sheath fold
Z
Y
X
Qz
Bt
1.6
1.4
1.2
1
0.8
0.6
2.5
2
1.5
1
0.5
Kernel density
Investigated sub-volumes
(0001)
(001)
17a-IV_2
17a-IV_4
17a-V_1
17a-III_3+4
17a-III_1+2
17a-V_1+2+3+4
17a-5
17a-II
17a-I
17a-III
17a-V
17a-IV

Fig. 12

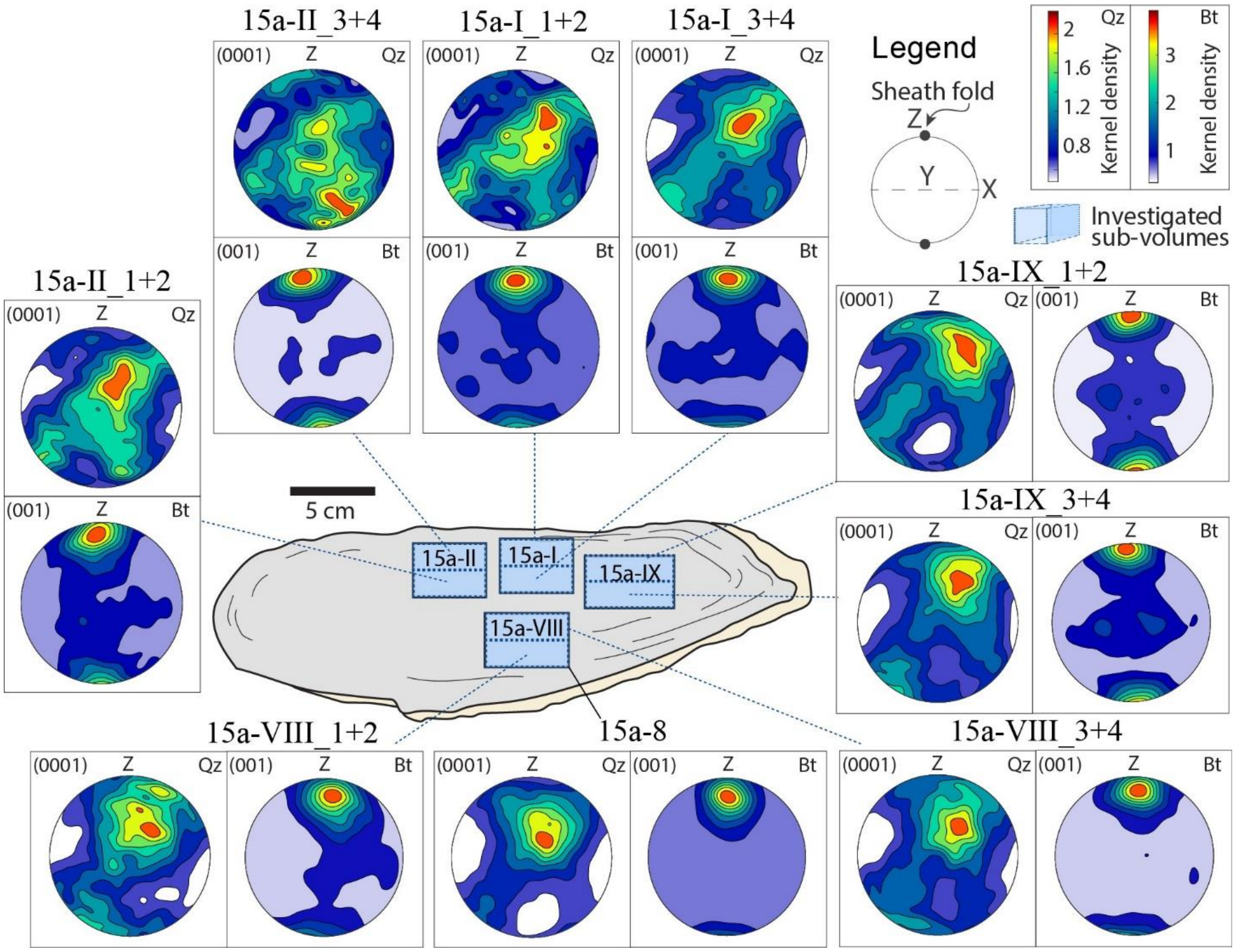
15a-II_3+4
15a-I_1+2
15a-I_3+4
Legend
Sheath fold
Z
Y
X
Investigated sub-volumes
Qz
Bt
Kernel density
15a-II_1+2
15a-IX_1+2
15a-IX_3+4
5 cm
15a-II
15a-I
15a-IX
15a-VIII
15a-8
15a-VIII_1+2
15a-VIII_3+4
(0001)
(001)

Fig. 13

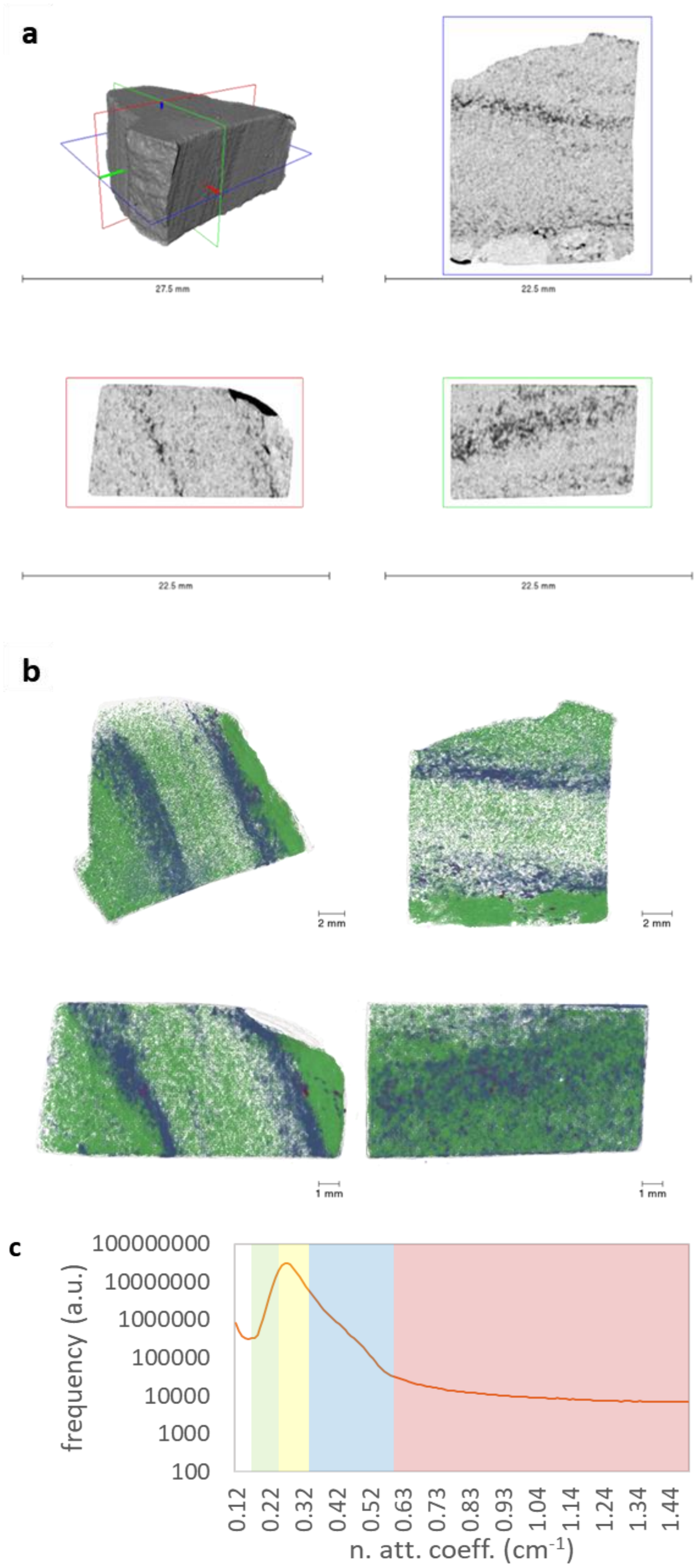

d

	matrix	p1	p2	p3
Mineral	Qtz+Pl	K-feld	?	Bt
Volume fraction(%)	80.130	10.271	9.253	0.306

Fig. 14

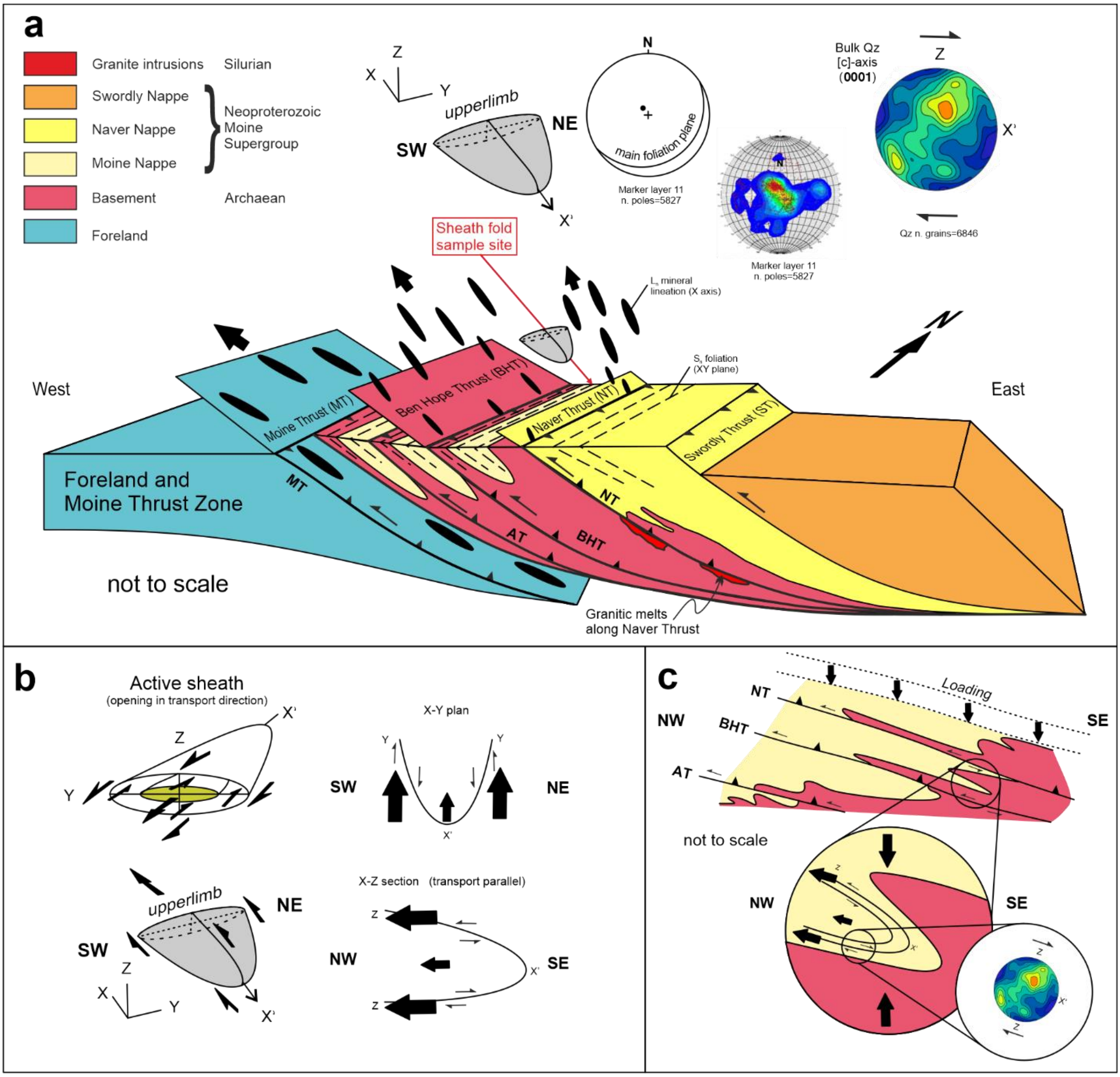
a
Granite intrusions
Silurian
Swordly Nappe
Naver Nappe
Moine Nappe
Neoproterozoic
Moine
Supergroup
Basement
Archaean
Foreland
upperlimb
SW
NE
main foliation plane
Marker layer 11
n. poles=5827
Bulk Qz
[c]-axis
(0001)
Qz n. grains=6846
Sheath fold
sample site
mineral lineation (X axis)
foliation (XY plane)
West
East
Moine Thrust (MT)
Ben Hope Thrust (BHT)
Naver Thrust (NT)
Swordly Thrust (ST)
Foreland and
Moine Thrust Zone
MT
AT
BHT
NT
not to scale
Granitic melts
along Naver Thrust
b
Active sheath
(opening in transport direction)
X-Y plan
X-Z section (transport parallel)
NW
SE
c
Loading
not to scale

Fig. 15

References

- Alsop, G. I., and Carreras, J., 2007. The structural evolution of sheath folds: A case study from Cap de Creus. Journal of Structural Geology, 29(12), 1915-1930.
- Alsop, G.I. 1992. Progressive deformation and the rotation of contemporary fold axes in the Ballybofey Nappe, northwest Ireland. Geological Journal 27, 271-283.
- Alsop, G.I., 1994. Relationships between distributed and localised shear in the tectonic evolution of a Caledonian fold and thrust zone, northwest Ireland. Geological Magazine 131, 123-136.
- Alsop, G.I., Cheer, D.A., Strachan, R.A., Krabbendam, M., Kinny, P.D., Holdsworth, R.E., Leslie, A.G., 2010. Progressive fold and fabric evolution associated with regional strain gradients: a case study from across a Scandian ductile thrust nappe, Scottish Caledonides. In: Law, R.D. (Ed.), Continental Tectonics and Mountain Building: The Legacy of Peach and Horne. Geological Society, London, Special Publications, vol. 335, pp. 253-272
- Alsop, G.I., Holdsworth, R.E., 1993. The distribution, geometry and kinematic significance of Caledonian buckle folds in the western Moine Nappe, northwestern Scotland. Geological Magazine 130, 353-362.
- Alsop, G.I., Holdsworth, R.E., 2004. The geometry and topology of natural sheath folds: a new tool for structural analysis. Journal of Structural Geology, 26(9), 1561-1589.
- Alsop, G.I., Holdsworth, R.E., 2006. Sheath folds as discriminators of bulk strain type, J. Struct. Geol. 28, 1588-1606
- Alsop, G.I., Holdsworth, R.E., 2007. Flow perturbation folding in shear zones. In: Ries, A.C., Butler, R.W.H. & Graham, R.D. (Eds) Deformation of the Continental Crust: The legacy of Mike Coward. Geological Society, London, Special Publications, 272, 77-103.
- Alsop, G.I., Holdsworth, R.E., 2012. The three dimensional shape and localisation of deformation within multilayer sheath folds. J. Struct. Geol. 44, 110–128.
- Alsop, G.I., Holdsworth, R.E., McCaffrey, K.J.W., 2007. Scale invariant sheath folds in salt, sediments and shear zones, J. Struct. Geol. 29, 1585-1604.
- Alsop, G.I., Holdsworth, R.E., Strachan, R.A., 1996. Transport-parallel cross folds within a mid-crustal Caledonian thrust stack, northern Scotland. J. Struct. Geol. 18, 783-790.
- Alsop, G.I., Strachan, R.A., Holdsworth, R.E., Burns, I.M., 2021. Geometry of folded and boudinaged pegmatite veins emplaced within a strike-slip shear zone: A case study from the Caledonian orogen, northern Scotland. J. Struct. Geol. 142, 104233. https://doi.org/10.1016/j.jsg.2020.104233

- Ashley, K.T., Thigpen, J.R., Law, R.D., 2015. Prograde evolution of the Scottish Caledonides and tectonic implications. Lithos 224–225, 160–178. https://doi.org/10.1016/j.lithos.2015.03.011
- Bons, P., Jansen, D., Mundel, F., Bauer, C. C., Binder, T., Eisen, O., ... and Weikusat, I., 2016. Converging flow and anisotropy cause large-scale folding in Greenland's ice sheet. Nat Commun 7, 11427. https://doi.org/10.1038/ncomms11427
- Bunge, H.J. 1982. Texture analysis in materials science, 1st Edition: mathematical methods. Butterworth-Heinemann, London, 614 pp.
- Carreras, J., Druguet, E., 2019. Complex fold patterns developed by progressive deformation. Journal of Structural Geology 125, 195–201. https://doi.org/10.1016/j.jsg.2018.07.015
- Carreras, J., Druguet, E., Griera, A., 2005. Shear zone-related folds. Journal of Structural Geology 27, 1229–1251. https://doi.org/10.1016/J.JSG.2004.08.004
- Carreras, J., Estrada, A., White, S., 1977. The effects of folding on the C-axis fabrics of a quartz mylonite. Tectonophysics 39, 3-24.
- Cobbold, P.R., Quinquis, H., 1980. Development of sheath folds in shear regimes. Journal of Structural Geology 2, 119-126
- Crispini L., Capponi, G., 1997. Quartz fabric and strain partitioning in sheath folds: an example from the Voltri Group (Western Alps, Italy). J. Struct. Geol. 19, 1149-1157.
- Cross, A. J., Prior, D. J., Stipp, M., Kidder, S., 2017. The recrystallized grain size piezometer for quartz: An EBSD- based calibration. Geophysical Research Letters, 44(13), 6667-6674. https://doi.org/10.1002/2017GL073836
- Davis, G. H., & Reynolds, S. J. (1996). Structural geology of rocks and regions. John Wiley & Sons.
- Druguet, E., Alsop, G.I., Carreras, J. 2009. Coeval brittle and ductile structures associated with extreme deformation partitioning in a multilayer sequence. Journal of Structural Geology 31, 498-511.
- Faleiros F.M., Moraes R., Pavan M., Campanha G.A.C., 2016. A new empirical calibration of the quartz c-axis fabric opening-angle deformation thermometer. Tectonophysics, 671, 7, 173-182, https://doi.org/10.1016/j.tecto.2016.01.014
- Fazio, E., 2019. Recognition of Structures in Mid-crustal Shear Zones and How to Discern Between Them, in: A. Billi, Å. Fagereng (Eds.), Problems and Solutions in Structural Geology and Tectonics, Elsevier, 2019: pp. 119–128. https://doi.org/10.1016/B978-0-12-814048-2.00010-7.
- Fazio, E., Ortolano, G. Visalli, R. Alsop, G.I, Cirrincione, R., Pezzino A., 2018. Strain localization and sheath fold development during progressive deformation in a ductile shear zone: a case study of macro- to microscale structures from the Aspromonte Massif, Calabria. Italian Journal of Geosciences, 137 (2): 208–218.

- Fazio, E., Punturo, R., Cirrincione, R., 2010. Quartz c-axis texture mapping of mylonitic metapelite with rod structures (Calabria, southern Italy): Clues for hidden shear flow direction. Journal of the Geological Society of India 75, 171–182. https://doi.org/10.1007/s12594-010-0006-z
- Fazio, E., Punturo, R., Cirrincione, R., Kern, H., Pezzino, A., Wenk, H.-R., Goswami, S., Mamtani, M.A., 2017. Quartz preferred orientation in naturally deformed mylonitic rocks (Montalto shear zone–Italy): a comparison of results by different techniques, their advantages and limitations. International Journal of Earth Sciences. https://doi.org/10.1007/s00531-016-1424-y
- Feldmann, K., 1989. Texture investigations by neutron time-of-flight diffraction. Textures Microstructures 10, 309–323.
- Fiduk, J.C., Rowan, M.G., 2012. Analysis of folding and deformation within layered evaporites in Blocks BM-S-8 & -9, Santos Basin, Brazil, in: Alsop, G.I., Archer, S.G., Hartley, A.J., Grant, N.T., Hodgkinson, R. (Eds.), Salt Tectonics, Sediments and Prospectivity. Geological Society of London, p. 0. https://doi.org/10.1144/SP363.22
- Garbe, U Randall T, Hughes C, Davidson G, Pangelis S, Kennedy SJ, 2015. A new neutron radiography/tomography/imaging station DINGO at OPAL, Physics Procedia 69, 27-32
- Ghosh, S.K., Hazra, S., Sengupta, S., 1999. Planar, non-planar and refolded sheath folds in the Phulad Shear Zone, Rajasthan, India. Journal of Structural Geology 21, 1715–1729. https://doi.org/10.1016/S0191-8141(99)00118-2
- Goddard, R. M., Hansen, L. N., Wallis, D., Stipp, M., Holyoke III, C. W., Kumamoto, K. M., & Kohlstedt, D. L., 2020. A subgrain- size piezometer calibrated for EBSD. Geophysical Research Letters, 47(23), e2020GL090056.
- Graziani, R., Larson, K.P., Law, R.D., Vanier, M.-A., Thigpen, J.R., 2021. A refined approach for quantitative kinematic vorticity number estimation using microstructures. Journal of Structural Geology 153, 104459. https://doi.org/10.1016/j.jsg.2021.104459
- Graziani, R., Larson, K.P., Soret, M., 2020. The effect of hydrous mineral content on competitive strain localization mechanisms in felsic granulites. Journal of Structural Geology 134, 104015. https://doi.org/10.1016/J.JSG.2020.104015
- Hielscher, R. & Schaeben, H. 2008. A novel pole figure inversion method: specification of the MTEX algorithm. Journal of Applied Crystallography, 41, 1024–1037.
- Holdsworth, R.E., 1989. The geology and structural evolution of a Caledonian fold and ductile thrust zone, Kyle of Tongue region, Sutherland, northern Scotland. Journal of the Geological Society, 146, 809-823.
- Holdsworth, R.E., Alsop, G.I., Strachan, R.A., 2007. Tectonic stratigraphy and structural continuity of the northernmost Moine Thrust Zone and Moine Nappe, Scottish Caledonides. In: Ries, A.C., Butler,

R.W.H., Graham, R.D. (Eds.), Deformation of the Continental Crust: The legacy of Mike Coward. Geological Society, London, Special Publications, vol. 272, pp. 123-144.

- Holdsworth, R.E., Grant, C.J., 1990. Convergence-related "dynamic spreading" in a mid-crustal ductile thrust zone: A possible orogenic wedge model. Geological Society Special Publication 54, 491–500. https://doi.org/10.1144/GSL.SP.1990.054.01.45
- Holdsworth, R.E., Strachan, R.A., Alsop, G.I., 2001. Geology of the Tongue District. Memoirs of the British Geological Survey, Sheet 114E(Scotland), p. 76.
- Holdsworth, R.E., Strachan, R.A., Alsop, G.I., Grant, C.J., Wilson, R.W., 2006. Thrust sequences and the significance of low-angle, out-of-sequence faults in the northernmost Moine Nappe and Moine Thrust Zone, NW Scotland. Journal of the Geological Society, London 163, 801-814.
- Holdsworth, R.E., Strachan, R.A., Harris, A.L., 1994. Precambrian rocks in northern Scotland east of the Moine Thrust: the Moine Supergroup. A revised correlation of Precambrian rocks in the British Isles 23–32.
- Hudec, M.R., Jackson, M.P.A., 2007. Terra infirma: Understanding salt tectonics. Earth-Science Reviews 82, 1–28. https://doi.org/10.1016/j.earscirev.2007.01.001
- Hunter, N.J.R., Luzin, V., Wilson, C.J.L., 2017a. Direct measurement of the quartz c-axis using neutron diffraction. Tectonophysics 712–713, 464–468. https://doi.org/10.1016/j.tecto.2017.05.019
- Hunter, N.J.R., Weinberg, R.F., Wilson, C.J.L., Law, R.D., 2018a. A new technique for quantifying symmetry and opening angles in quartz c-axis pole figures: Implications for interpreting the kinematic and thermal properties of rocks. J. Struct. Geol. 112, 1–6. https://doi.org/10.1016/j.jsg.2018.04.006
- Hunter, N.J.R., Weinberg, R.F., Wilson, C.J.L., Luzin, V., Misra, S., 2018b. Microscopic anatomy of a "hot-on-cold" shear zone: Insights from quartzites of the Main Central Thrust in the Alaknanda region (Garhwal Himalaya). Bull. Geol. Soc. Am. 130, 1519–1539. https://doi.org/10.1130/B31797.1
- Hunter, N.J.R., Wilson, C.J.L., Luzin, V., 2017b. Comparison of quartz crystallographic preferred orientations identified with optical fabric analysis, electron backscatter and neutron diffraction techniques. J. Microsc. 265, 169–184. https://doi.org/10.1111/jmi.12472
- Jackson, M. P. A., Vendeville, B. C., and Sharp, I. R., 1994. "Salt tectonics: a global perspective." AAPG Memoir 65: 51-70.
- Kampmann, T. C., Stephens, M. B., & Weihed, P., 2016. 3D modelling and sheath folding at the Falun pyritic Zn-Pb-Cu-(Au-Ag) sulphide deposit and implications for exploration in a 1.9 Ga ore district, Fennoscandian Shield, Sweden. Mineralium Deposita, 51, 665-680. https://doi.org/10.1007/s00126-016-0638-z.
- Krabbendam, M., Leslie, A.G. 1996. Folds with vergence opposite to the sense of shear. Journal of Structural Geology 18, 777-781.

- Kruhl, J.H., 1996. Prism- and basal-plane parallel subgrain boundaries in quartz: a microstructural geothermobarometer. Journal of Metamorphic Geology 14, 581–589. https://doi.org/10.1046/j.1525-1314.1996.00413.x
- Law, R.D., 2014. Deformation thermometry based on quartz c-axis fabrics and recrystallization microstructures: A review. Journal of Structural Geology, 66, 129-161. https://doi.org/10.1016/j.jsg.2014.05.023
- Law, R.D., Thigpen, J.R., Mazza, S.E., Mako, C.A., Krabbendam, M., Spencer, B.M., Ashley, K.T., Strachan, R.A., Davis, E.F., 2021. Tectonic Transport Directions, Shear Senses and Deformation Temperatures Indicated by Quartz c-Axis Fabrics and Microstructures in a NW-SE Transect across the Moine and Sgurr Beag Thrust Sheets, Caledonian Orogen of Northern Scotland. Geosciences 11. https://doi.org/10.3390/geosciences11100411
- Maino, M., Adamuszek, M., Schenker, F.L., Seno, S., Dabrowski, M., 2021. Sheath fold development around deformable inclusions: Integration of field-analysis (Cima Lunga unit, Central Alps) and 3D numerical models. Journal of Structural Geology 144, 104255. https://doi.org/10.1016/j.jsg.2020.104255
- Merschat, A.J., Hatcher Jr,R.D., Davis, T.L. 2005. The northern Inner Piedmont, southern Appalachians, USA: kinematics of transpression and SW-directed mid-crustal flow. Journal of Structural Geology, 27(7), 1252-1281. https://doi.org/10.1016/j.jsg.2004.08.005
- Michels, Z.D., Kruckenberg, S.C., Davis, J.R., Tikoff, B., 2015. Determining vorticity axes from grain-scale dispersion of crystallographic orientations. Geology 43, 803–806. https://doi.org/10.1130/G36868.1
- Micieli, D. Minniti, T. Gorini, G. (2019) NeuTomPy toolbox, a Python package for tomographic data processing and reconstruction, SoftwareX, 9, 260-264, https://doi.org/10.1016/j.softx.2019.01.005.
- Minnigh, L.D., 1979. Structural analysis of sheath folds in a meta-chert from the western Italian Alps. Journal of Structural Geology 1, 275-282.
- Morales, L.F.G., Casey, M., Lloyd, G.E., Williams, D.M., 2011a. Kinematic and temporal relationships between parallel fold hinge lines and stretching lineations: A microstructural and crystallographic preferred orientation approach. Tectonophysics 503, 207–221. https://doi.org/10.1016/j.tecto.2011.03.003
- Morales, L.F.G., Mainprice, D., Lloyd, G.E., Law, R.D., 2011b. Crystal fabric development and slip systems in a quartz mylonite: An approach via transmission electron microscopy and viscoplastic self-consistent modelling, Geological Society Special Publication. https://doi.org/10.1144/SP360.9
- Morgan S.S., Law, R.D. (2004) Unusual transition in quartzite dislocation creep regimes and crystal slip systems in the aureole of the Eureka Valley–Joshua Flat–Beer Creek plúton, California: a case for anhydrous conditions created by decarbonation reactions. Tectonophysics, 384, 209-231, https://doi.org/10.1016/j.tecto.2004.03.016

- Mudruk, S.V., Balagansky, V.V., Raevsky, A.B., Rundkvist, O.V., Matyushkin, A.V., Gorbunov, I.A., 2022. Complex shape of the Palaeoproterozoic Serpovidny refolded mega-sheath fold in northern Fennoscandia revealed by magnetic and structural data. Journal of Structural Geology 154, 104492. https://doi.org/10.1016/j.jsg.2021.104492
- Nania, L., Montomoli, C., Iaccarino, S., Leiss, B., Carosi, R., 2022. Multi-stage evolution of the South Tibetan Detachment System in central Himalaya: Insights from carbonate-bearing rocks. Journal of Structural Geology 158, 104574. https://doi.org/10.1016/J.JSG.2022.104574
- Neumann, B. (2000). Texture development of recrystallised quartz polycrystals unravelled by orientation and misorientation characteristics. Journal of Structural Geology, 22(11-12), 1695-1711. https://doi.org/10.1016/S0191-8141(00)00060-2.
- Oriolo, S., Schulz, B., Hueck, M., Oyhantçabal, P., Heidelbach, F., Sosa, G., van den Kerkhof, A., Wemmer, K., Fossen, H., Druguet, E., Walter, J., Cavalcante, C., Siegesmund, S., 2022. The petrologic and petrochronologic record of progressive vs polyphase deformation: Opening the analytical toolbox. Earth-Science Reviews 234. https://doi.org/10.1016/j.earscirev.2022.104235
- Ortolano, G., Fazio, E., Visalli, R., Alsop, G.I., Pagano, M., Cirrincione, R., 2020. Quantitative microstructural analysis of mylonites formed during Alpine tectonics in the western Mediterranean realm. Journal of Structural Geology 131. https://doi.org/10.1016/j.jsg.2019.103956
- Park, A.F., 1988. Geometry of sheath folds and related fabrics at the Luikonlahti mine, Svecokarelides, eastern Finland. Journal of Structural Geology 10(5), 487-498. https://doi.org/10.1016/0191-8141(88)90036-3.
- Passchier, C. W., & Trouw, R. A. J. (2005). Microtectonics. Springer Science & Business Media.
- Pérez-Valera, F., M. Sánchez-Gómez, A. Pérez-López, and L. A. Pérez-Valera (2017), An evaporite-bearingaccretionary complex in the northernfront of the Betic-Rif orogen, Tectonics, 36, 1006–1036, doi:10.1002/2016TC004414.
- Piette-Lauzière N., Larson, K.P. Kellett, D.A. Graziani, R. (2020), Intracrystalline vorticity record of flow kinematics during shear zone reactivation, Journal of Structural Geology, 140,104134, https://doi.org/10.1016/j.jsg.2020.104134.
- Punturo, R., Mamtani, M.A., Fazio, E., Occhipinti, R., Renjith, A.R., Cirrincione, R., 2017. Seismic and magnetic susceptibility anisotropy of middle-lower continental crust: Insights for their potential relationship from a study of intrusive rocks from the Serre Massif (Calabria, southern Italy). Tectonophysics 712–713, 542–556. https://doi.org/10.1016/j.tecto.2017.06.020
- Quinquis, H., Audren, C., Brun, J.P., Cobbold, P., 1978. Intensive progressive shear in Ile de Groix blueschists and compatibility with subduction or obduction. Nature 274, 43-45.
- Ramsay, J. G. (1967). "Folding and Fracturing of Rocks." McGraw-Hill, New York.

- Ramsay, J. G., and Huber, M. I. (1987). "The Techniques of Modern Structural Geology, Volume 2: Folds and Fractures." Academic Press, London.
- Ramsay, J.G., 1980. Shear zone geometry: a review. Journal of Structural Geology 2, 83-99.
- Ramsay, J.G., Huber, M.I., 1983. The techniques of modern structural geology. Volume 1, “Strain analysis” Academic Press, London.
- Reber, J.E., Dabrowski, M., Galland, O., Schmid, D.W., 2013a. Sheath fold morphology in simple shear. Journal of Structural Geology 53, 15–26. https://doi.org/10.1016/J.JSG.2013.05.003
- Reber, J.E., Dabrowski, M., Schmid, D.W., 2012. Sheath fold formation around slip surfaces. Terra Nova 24. https://doi.org/10.1111/j.1365-3121.2012.01081.x
- Reber, J.E., Galland, O., Cobbold, P.R., Veslud, C.L.C. de, 2013b. Experimental study of sheath fold development around a weak inclusion in a mechanically layered matrix. Tectonophysics 586, 130–144. https://doi.org/10.1016/J.TECTO.2012.11.013
- Reddy, G.P.O., 2018. Digital Image Processing: Principles and Applications. In: Reddy, G., Singh, S. (eds) Geospatial Technologies in Land Resources Mapping, Monitoring and Management. Geotechnologies and the Environment, vol 21. Springer, Cham. https://doi.org/10.1007/978-3-319-78711-4_6
- Renjith, A.R., Mamtani, M.A., Urai, J.L., 2016. Fabric analysis of quartzites with negative magnetic susceptibility – Does AMS provide information of SPO or CPO of quartz? Journal of Structural Geology 82, 48–59. https://doi.org/10.1016/j.jsg.2015.11.005
- Roberts, R.G., 1987. Ore deposit models# 11. Archean lode gold deposits. Geoscience Canada, 14(1), 37-52.
- Rosas, F., Marques, F.O., Luz, A., Coelho, S., 2002. Sheath folds formed by drag induced by rotation of rigid inclusions in viscous simple shear flow: nature and experiment. Journal of Structural Geology 24, 45–55. https://doi.org/10.1016/S0191-8141(01)00046-3
- Rowan, M.G., Vendeville, B.C., 2006. Foldbelts with early salt withdrawal and diapirism: Physical model and examples from the northern Gulf of Mexico and the Flinders Ranges, Australia. Marine and Petroleum Geology 23, 871–891. https://doi.org/10.1016/j.marpetgeo.2006.08.003
- Schaeben, H. 1997. A simple standard orientation density function: the hyperspherical de la Vall´ee Poussin kernel. Physica status solidi (b), 200, 367–376. https://doi.org/10.1002/1521-3951(199704)200:2<367::AID-PSSB367>3.0.CO;2-I.
- Schmid, S.M., Casey, M., 1986. Complete fabric analysis of some commonly observed quartz c-axis patterns. Mineral and Rock Deformation: Laboratory Studies 36, 263–286.

- Schulz, B., Steenken, A., & Siegesmund, S., 2008. Geodynamic evolution of an Alpine terrane—the Austroalpine basement to the south of the Tauern window as a part of the Adriatic Plate (eastern Alps). Geological Society, London, Special Publications, 298(1), 5-44.
- Searle, M.P., Alsop, G.I., 2007. Eye to eye with a mega-sheath fold: case study from Wadi Mayh, northern Oman Mountains. Geology 35, 1043-1046.
- Skemer, P., Katayama, I., Jiang, Z. & Karato, S.I. 2005. The misorientation index: development of a new method for calculating the strength of lattice-preferred orientation. Tectonophysics, 411, 157–167. https://doi.org/10.1016/j.tecto.2005.08.023.
- Southern, S.C., Mosher, S., and Orlandini, O.F., 2022, Strain partitioning in the Moine Nappe, northernmost Scotland: Geosphere, v. 19, no. 1, p. 47–74, https://doi.org/10.1130/GES02522.1.
- Stipp, M., Stünitz, H., Heilbronner, R., Schmid S.M., 2002. The eastern Tonale fault zone: a 'natural laboratory' for crystal plastic deformation of quartz over a temperature range from 250 to 700 °C. Journal of Structural Geology, 24, Issue 12, 1861-1884. https://doi.org/10.1016/S0191-8141(02)00035-4
- Strachan, R.A., Smith, M., Harris, A.L., Fettes, D. J., Trewin, N.H., 2002. The geology of Scotland. Geological Society, London.
- Strachan, R.A., Alsop, G.I., Ramezani, J., Frazer, R.E., Burns, I., Holdsworth, R.E., 2020. Patterns of Silurian deformation and magmatism during sinistral oblique convergence, northern Scottish Caledonides. J. Geol. Soc. 177, 893-910.
- Strachan, R.A., Holdsworth, R.E., Krabbendam, M., Alsop, G.I., 2010. The Moine Supergroup of NW Scotland: insights into the analysis of polyorogenic supracrustal sequences. In: Law, R.D., Butler, R.W.H., Holdsworth, R.E., Krabbendam, M., Strachan, R.A. (Eds.), Continental Tectonics and Mountain Building: The Legacy of Peach and Horne. Geological Society, London, Special Publications, vol. 335, pp. 231-252.
- Stünitz, H., 1991. Folding and shear deformation in quartzites, inferred from crystallographic preferred orientation and shape fabrics. Journal of Structural Geology, 13, 71-86. https://doi.org/10.1016/0191-8141(91)90102-O.
- Thigpen, J.R., Law, R.D., Loehn, C.L., Strachan, R.A., Tracy, R.J., Lloyd, G.E., Roth, B.L. and Brown, S.J., 2013. Thermal structure and tectonic evolution of the Scandian orogenic wedge, Scottish Caledonides: integrating geothermometry, deformation temperatures and conceptual kinematic-thermal models. J. Meta. Geol., 31: 813-842. https://doi.org/10.1111/jmg.12046
- Toy, V.G., Prior, D.J., Norris, R.J., 2008. Quartz fabrics in the Alpine Fault mylonites: Influence of pre-existing preferred orientations on fabric development during progressive uplift. Journal of Structural Geology 30, 602–621. https://doi.org/10.1016/j.jsg.2008.01.001

- Vogel, S.C., Priesmeyer, H.-G., 2006. 2. Neutron Production, Neutron Facilities and Neutron Instrumentation, in: Wenk, H.R. (Ed.), Neutron Scattering in Earth Sciences. De Gruyter, Berlin, Boston, pp. 27–58. https://doi.org/doi:10.1515/9781501509445-007
- Wheeler, J., Prior, D. J., Jiang, Z., Spiess, R., Trimby, P. W., 2001. The petrological significance of misorientations between grains. Contributions to mineralogy and petrology, 141(1), 109. https://doi.org/10.1007/s004100000225.
- Wilson, C. J. L. Hunter N. J. R. & Luzin V., 2022. Crystallographic preferred orientation of quartz deformed at granulite conditions: the Kalinjala Shear Zone, Port Neill, South Australia, Australian Journal of Earth Sciences, 69:8, 1119-1131, DOI: 10.1080/08120099.2022.2076740

Data availability

Datasets related to this article can be found at: https://data.mendeley.com/datasets/4byk4ycc2k/draft?a=14d00a06-90f3-4a90-aa90-83c7ad9c7dbb , an open-source online data repository hosted at Mendeley Data.

Appendix A. Supplementary material

A) 3D model: rendering of sheath fold shape (MOVE) – marker inner layers.

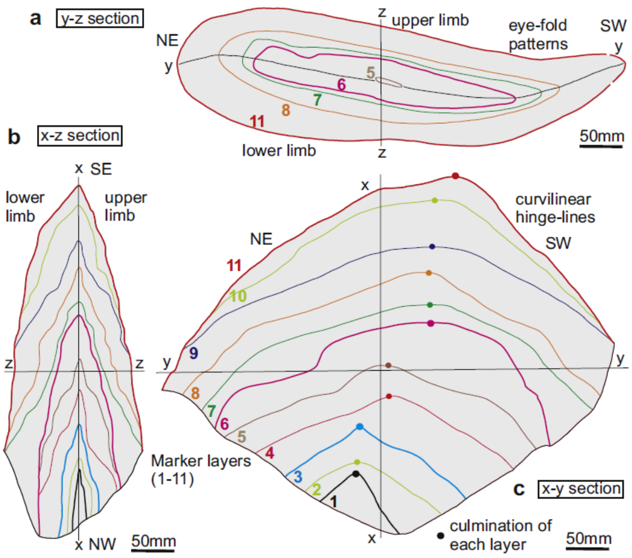

Supp. Fig.1 - Section views used for the 3D model (Alsop and Holdsworth, 2012). Marker layers have been plotted with MOVE software.

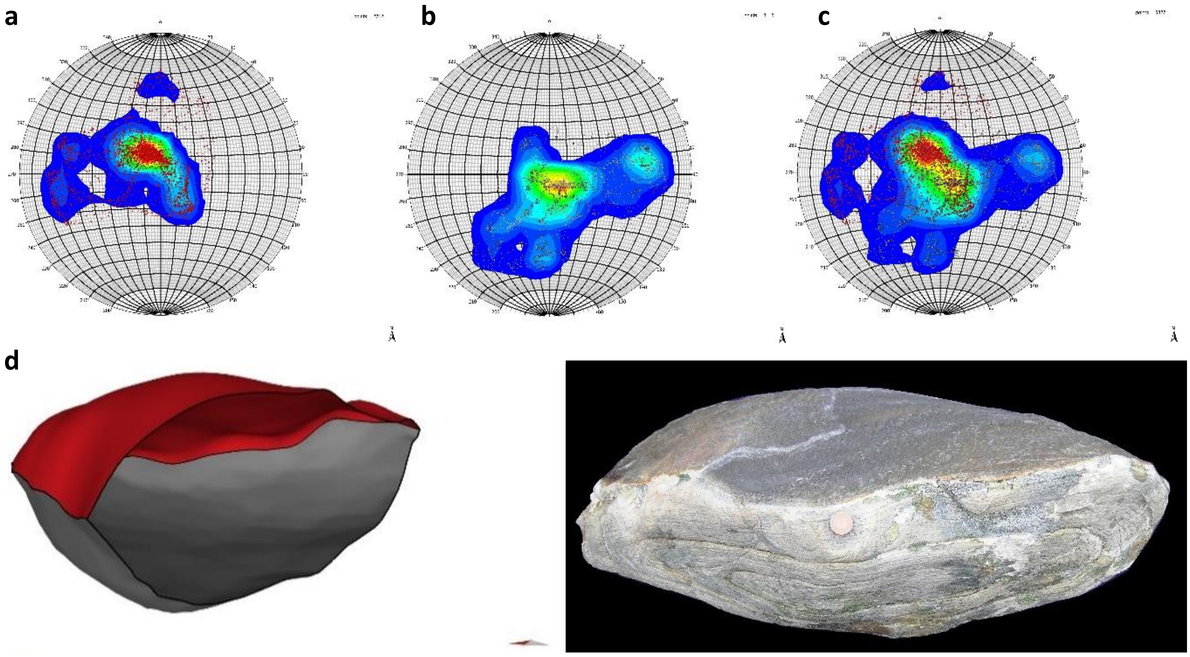

Supp. Fig. 2 - Stereo data extracted from reconstructed 3D virtual surface of the outermost folded foliation (smoothed version of marker layer n. 11 traced after Alsop and Holdsworth, 2002); poles of faces constituting the upper (red) and lower (gray) limb: a) upper limb (2712 poles); b) lower limb (3115 poles); c) upper & lower limbs together (5827 poles). The stereo data are plotted considering the actual sheath fold orientation (apex to SE). d) investigated sheath fold sample (see Alsop and Holdsworth, 2012).

B) Neutron diffraction (ND)

Neutron tomography of samples taken from different domains (18a-3; 17a-5; 16a-4; 15a-8) and reference frame.

Four specimens (15a-8; 16a-4; 17a-5; 18a-3; size ca. 15x15x15 mm) have been investigated to retrieve mineral phases 3D spatial distribution (for instrumental detailed information please refer to Garbe, et al., 2015) at ANSTO laboratory. We used the ANDOR MARANA (2048*2048) sCMOS sensor camera with the following settings: 30 µm thick Gadox scintillation screen; Pixel size: 17 mm; Step angle: 0.17°; Projection #: 1060; Exposure time: 90s; actual spatial resolution of~50 mm (Siemens star spoke target).

Data have been prepared by means of Neutompy Software to correct dark and bright spots and have been processed and reconstructed by the Octopus Software for flat field normalization, flux fluctuation, and dark current correction; tilt and rotation axis correction; Fourier Back Projection Radon Transform; ring artefacts suppression in frequency and real space domains. Finally, data have been visualized and evaluated (anisotropic diffusion; unsharp masking; threshold segmentation) by means of the AVIZO Software.

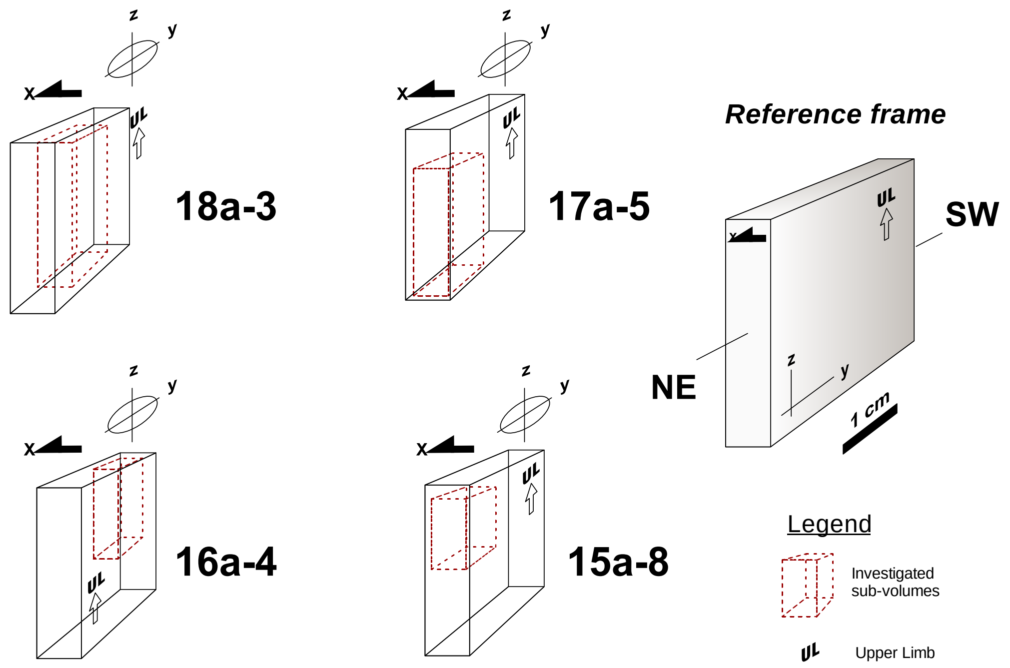

Supp. Fig. 3 – Rock sub-volumes and reference frame for the four investigated specimens.

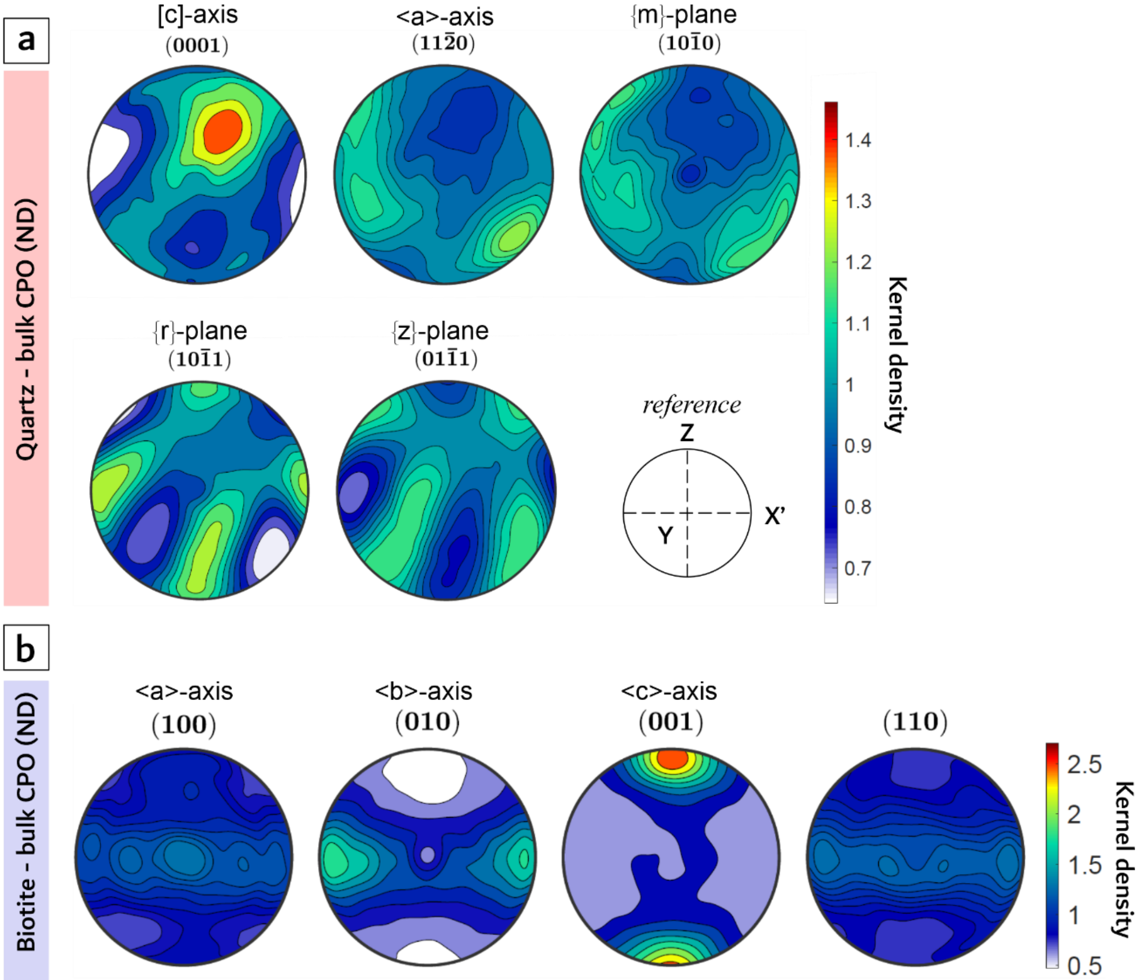

Supp. Fig. 4 – Bulk CPO inferred by means of Neutron Diffraction technique of a) quartz and b) biotite grains.

C) For paleo-stress:

a. EBSD maps with highlighted grains and vertical lines used to count subgrains for the paleo-stress calculation (see 'Data availability' section for download information);

b. grain size distribution maps with all grain size distribution graphs;

c. table with all the paleo-piezometry results from both the subgrains method and grain size distribution;

b. Grain size distributions histograms

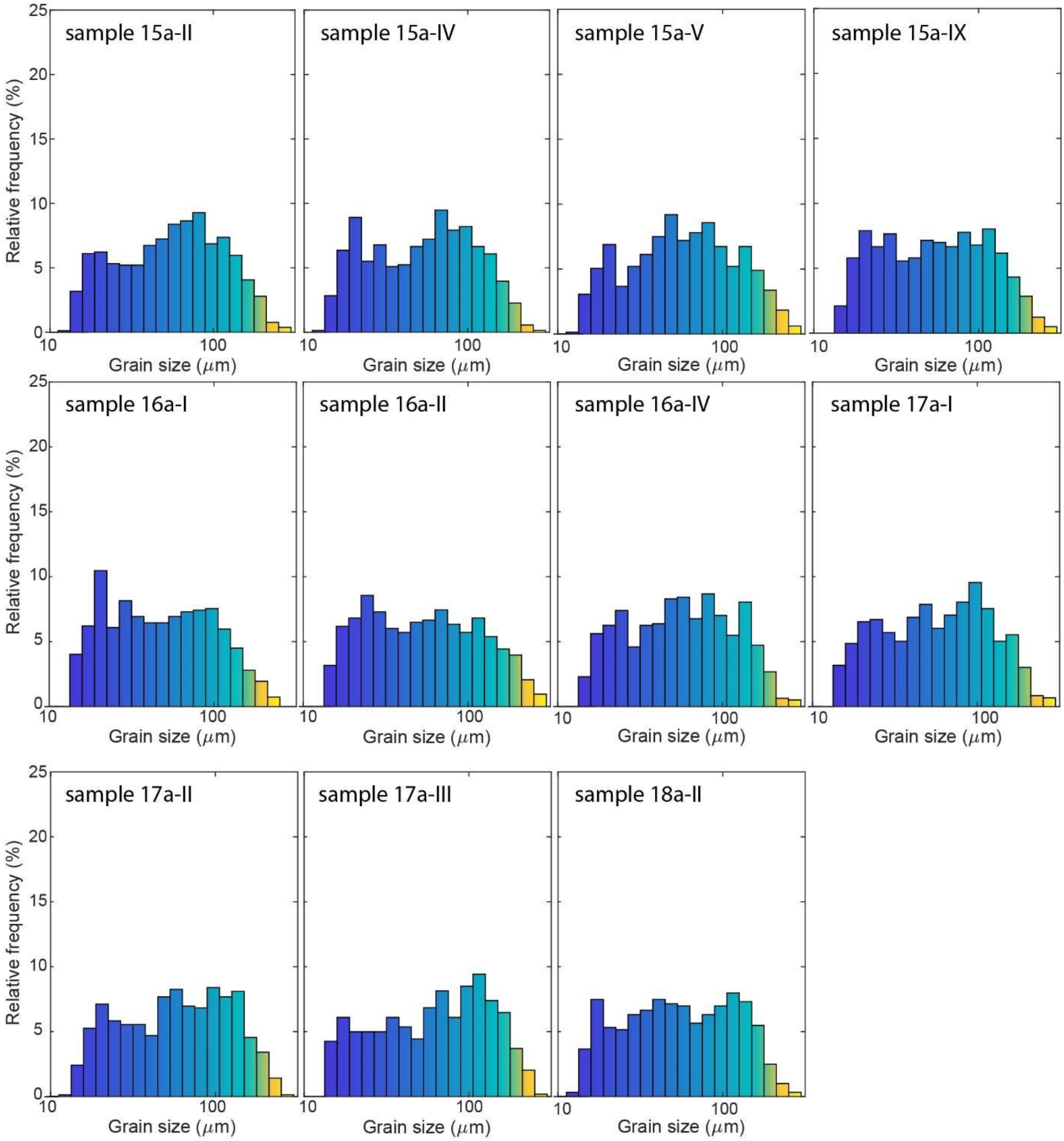

Grain size distributions maps – 01 – samples 15a, 16a

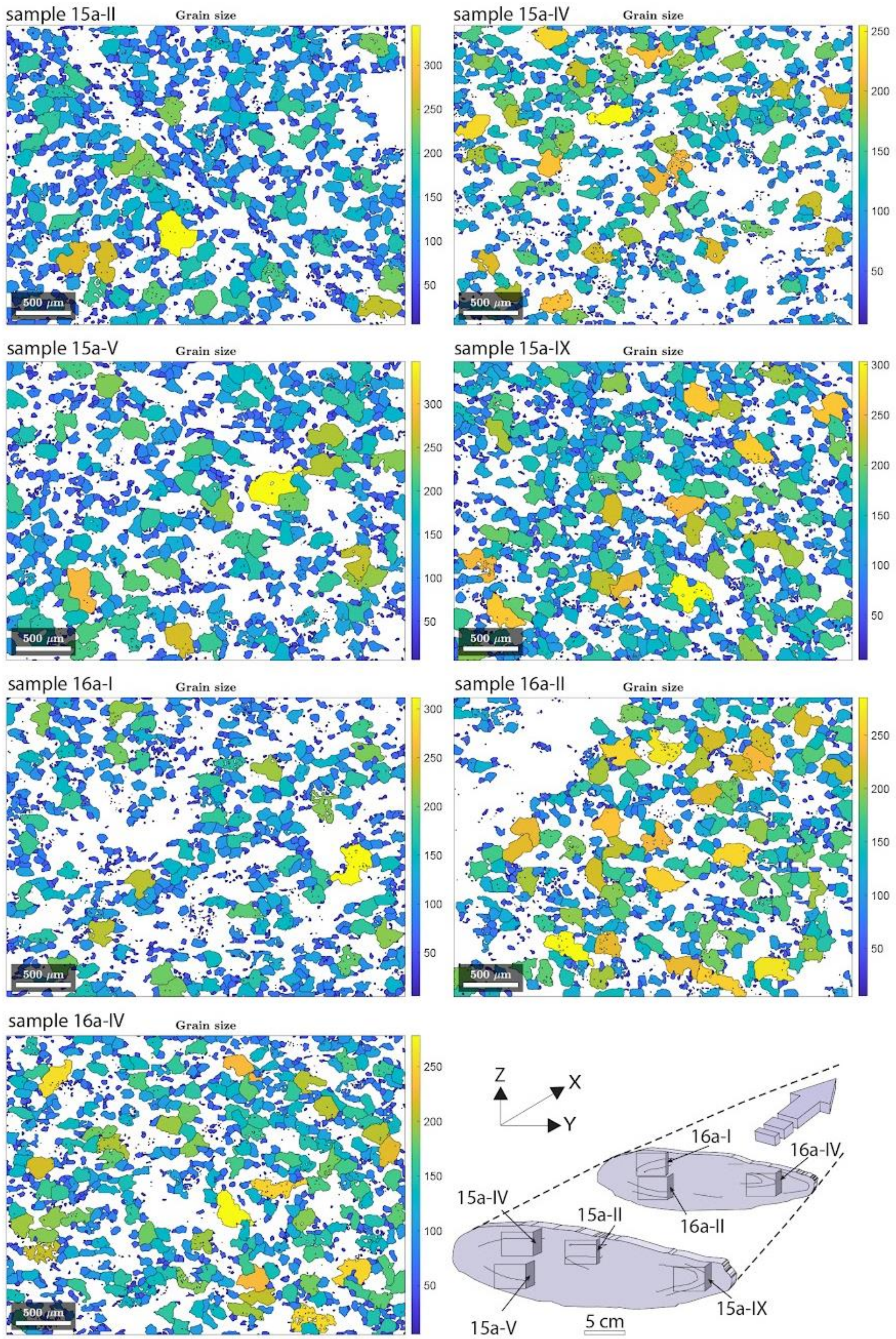

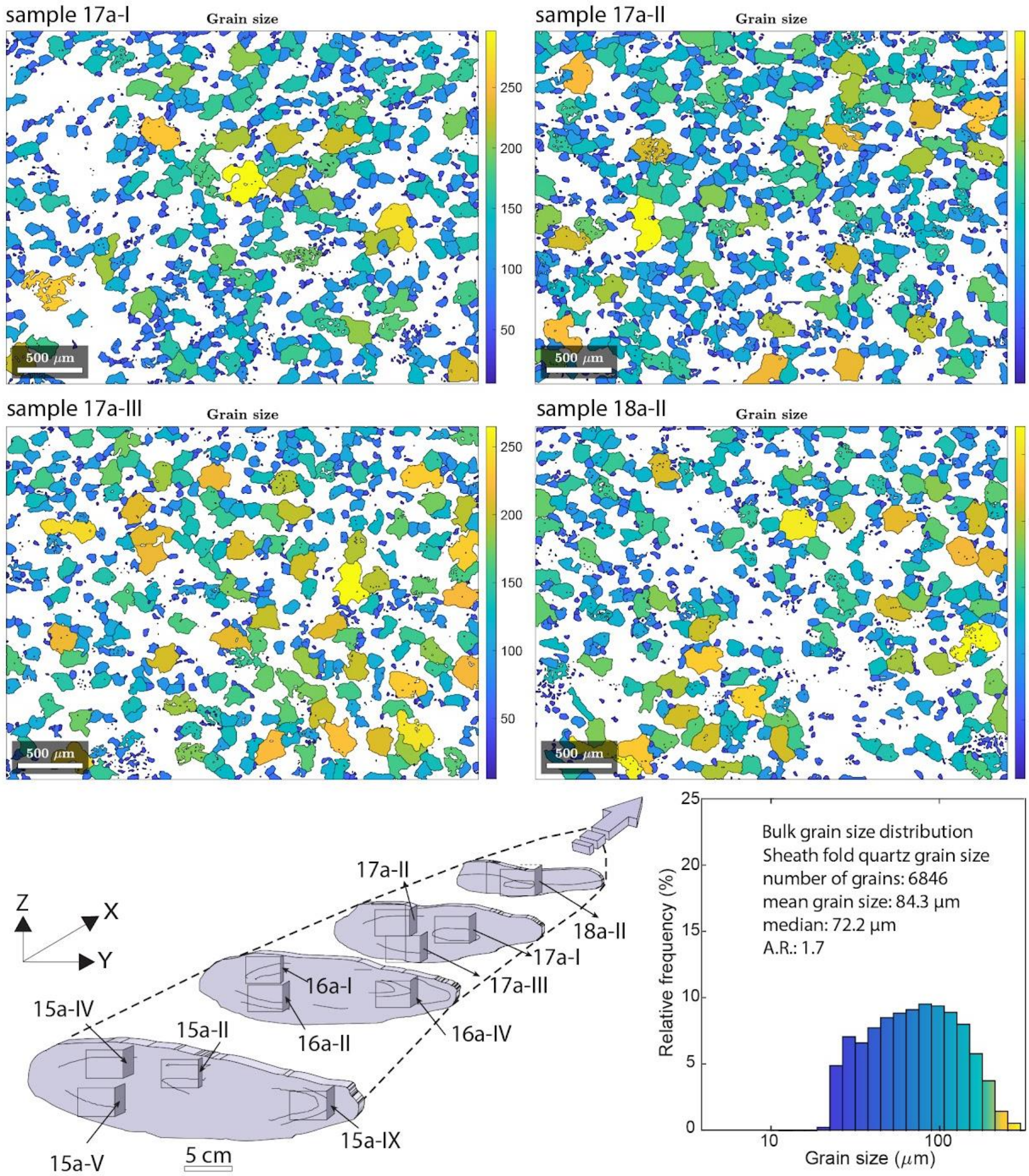

Grain size distributions maps – 02 – samples 17a, 18a

CPO data though the ND:

Table S1.

Sample	Quartz J-index	Quartz M-index	Biotite J-index	Biotite M-index
15a_8	1.24	0.019	1.46	0.022
15a_II_1_2	1.15	0.008	1.39	0.022
15a_II_3_4	1.13	0.006	1.59	0.024
15a_IX_1_2	1.17	0.009	1.47	0.018
15a_IX_3_4	1.18	0.010	1.46	0.019
15a_I_1_2	1.17	0.008	1.33	0.019
15a_I_3_4	1.24	0.013	1.40	0.019
15a_VIII_1_2	1.21	0.013	1.36	0.020
15a_VIII_4_5	1.23	0.014	1.42	0.019
17a_5	1.10	0.007	1.20	0.013
17a_III_1_2	1.10	0.006	1.17	0.013
17a_III_3_4	1.08	0.004	1.31	0.016
17a_II_1	1.06	0.003	1.58	0.042
17a_II_3	1.14	0.008	1.92	0.057
17a_IV_2	1.06	0.004	1.69	0.040
17a_IV_4	1.11	0.007	2.15	0.073
17a_I_1_2	1.12	0.010	1.60	0.044
17a_I_3_4	1.06	0.003	1.58	0.042
17a_V_1_2_3_4	1.11	0.007	1.35	0.029
17a_V_1	1.06	0.002	1.56	0.038

Table S1. Summary of the CPOs strengths for quartz and biotite after neutron diffraction investigations. CPOs strengths are expressed by the J-Index (or "texture index", Bunge, 1982) and the M-Index (Skemer et al., 2005).

Table S2.

Sample	lower left	lower right	Upper right	Upper left	Lower	Upper	OA	T°C (at 4.5 kbar) ±50 °C	Fabric
15a-II	32	111	219	312	79	93	86	578	Type I cross-girdle
15a-IX	40	141	220	319	101	99	100	640	cleft girdle (decentred)
16a-I	52	137	232	316	85	84	84,5	570	Type I cross-girdle

16a-IV	45	137	242	320	92	78	85	573	Type II cross-girdle
17a-II	44	150	236	303	106	67	87	580	Type II cross-girdle
Bulk	45	132	241	314	87	73	80	548	Type I cross-girdle

Bulk CVA

D) For CPO:

a. Pole figures with respect to the structural domain, both EBSD and Neutron diffractometer;

b. All CVAs

c. Misorientation angle degree diagrams to show the CPO strength.

Highlights

- We investigate the 3D geometry and kinematics to determine potential flow variation within sheath folds
- CPOs of quartz and biotite are acquired through a Neutron Diffractometer and an SEM-EBSD system
- CPO maintains constant shear sense throughout the fold with no evidence of active folding preserved
- Top-to-SE normal-shear sense within the sheath fold is opposite to the regional thrust kinematics and suggests a late phase of peak temperature extension.

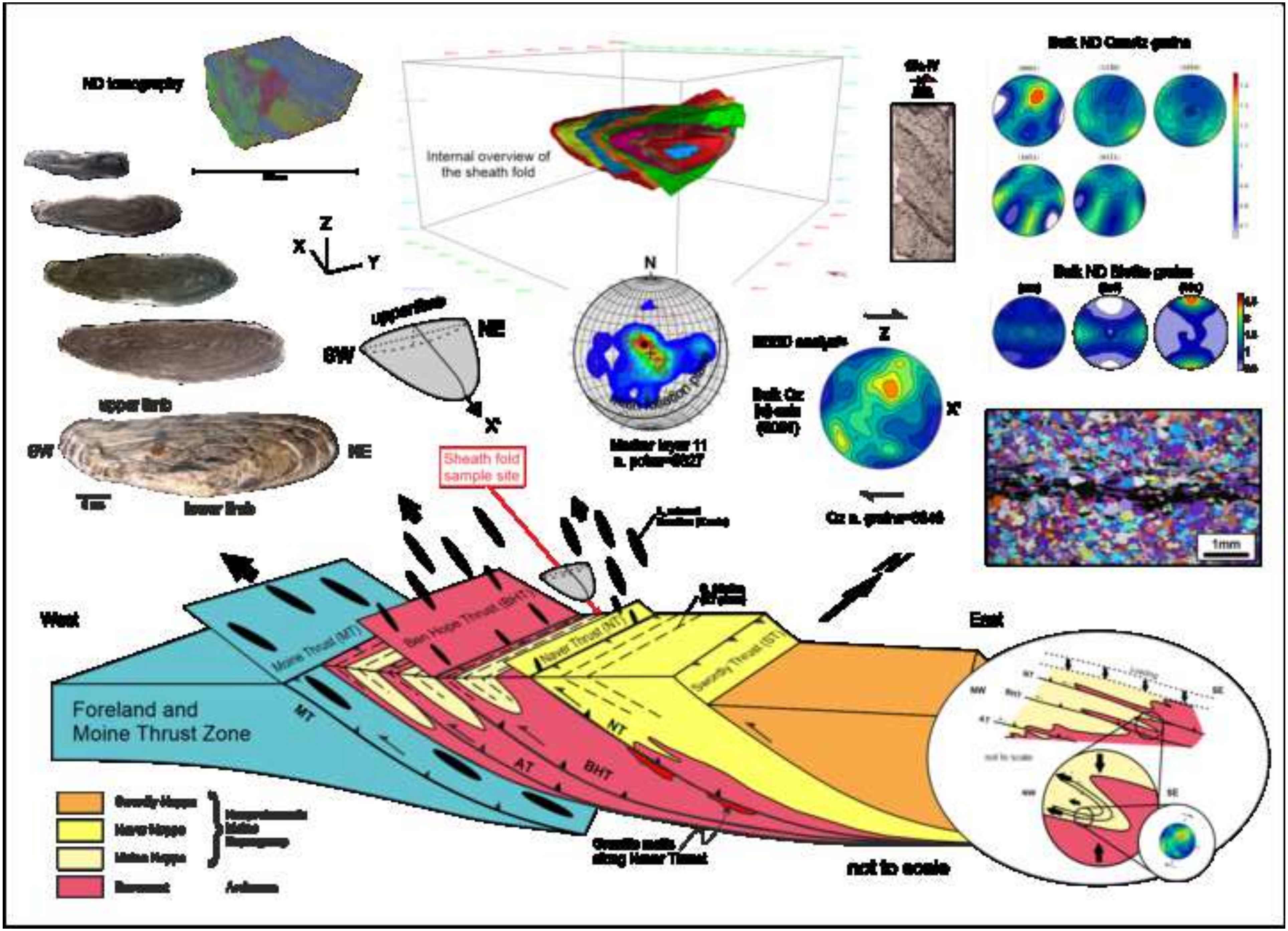
Internal overview of the sheath fold
Z
X
Y
upper limb
lower limb
SW
NE
X'
N
Sheath fold sample site
West
East
Foreland and Moine Thrust Zone
Moine Thrust (MT)
Ben Hope Thrust (BHT)
Naver Thrust (NT)
MT
AT
BHT
NT
not to scale
1mm